

Copyright  
by  
Yong J. Lee  
2006

The Dissertation Committee for Yong J. Lee  
certifies that this is the approved version of the following dissertation:

**Construction of a Low Temperature Nuclear Magnetic  
Resonance Force Microscope**

Committee:

---

John T. Markert, Supervisor

---

Chih-Kang Ken Shih

---

Alejandro de Lozanne

---

Zhen Yao

---

Li Shi

**Construction of a Low Temperature Nuclear Magnetic  
Resonance Force Microscope**

by

**Yong J. Lee, B.S.**

**DISSERTATION**

Presented to the Faculty of the Graduate School of  
The University of Texas at Austin  
in Partial Fulfillment  
of the Requirements  
for the Degree of

**DOCTOR OF PHILOSOPHY**

THE UNIVERSITY OF TEXAS AT AUSTIN

August 2006

Dedicated to my Lord Jesus Christ and to my family.

## Acknowledgments

The past 7 years at the University of Texas at Austin were a truly amazing part of my life. I met my wife, Soyeun, and many other life-long friends. It sure seems like I started my graduate education only a short time ago, but already seven years have passed. What can I say? Time really flies.

I do need to thank Dr. John T. Markert for his endless support during my research. I have learned so much while I was a part of his laboratory. Everything from cryogenics to NMR to superconductivity, I owe all to him. He was and still is such an approachable person even with a simple question. He always had one or two answers to my questions whether they were about the construction of the experimental apparatus or just some physics questions. I am forever indebted to him for everything I learned as a graduate student.

I must mention my wife, Soyeun, for her support throughout my graduate career. We had both happy and not-so-happy moments, but she was always there to help me in any way she could. We celebrated the birth of our first baby, Junhyung Jonathan Lee, this past February. And indeed Soyeun's and my lives have changed forever.

I also want to thank Dr. Daejin Eom for just being around so that I could talk to him and for encouraging me and helping me with many technical details of experiments and physics in general. He was and still is one of the brightest physicists that I've ever met. I hope his voyage in life will be very fruitful.

My thanks to all Markert lab members. I am particularly indebted to Wei Lu. He and I shared many hours of frustration and joy. I cannot think of any part of my setup that does not have his touch. Thank you Wei! Also special thanks to Han-Jong who gladly helped me in many ways. Keeseong and I had many interesting conversations in the office about superconductivity to highly correlated electron materials. He is the only person in the lab that is not directly involved in NMRFM, but his interest in the subject offered insights and suggestions that were helpful as I struggled with the experiment. Thank you Keeseong. I should thank Rosie for letting me borrow her electronics. She was always cooperative and supportive in my experiment. All other members of Markert lab are sincerely appreciated for their support.

# Construction of a Low Temperature Nuclear Magnetic Resonance Force Microscope

Publication No. \_\_\_\_\_

Yong J. Lee, Ph.D.

The University of Texas at Austin, 2006

Supervisor: John T. Markert

All aspects of a nuclear magnetic resonance force microscope (NM-RFM) have been constructed. The development and testing of each aspect area are discussed in detail. In particular, two sets of three-axis piezoelectric positioners based on a stick-slip motion have been successfully incorporated and tested for a wide temperature range. How each component of the microscope contributes to the signal measurement process is discussed, and possible solutions to unsuccessful attempts in detecting a spin-induced NMRFM signal are presented. Also, a novel, two-step phase cycling technique to eliminate the contribution to the spin signal from a spurious frequency modulated (FM) radiofrequency (RF) field, which can be utilized in future experiments, is discussed in detail.

# Table of Contents

<b>Acknowledgments</b>	<b>v</b>
<b>Abstract</b>	<b>vii</b>
<b>List of Tables</b>	<b>x</b>
<b>List of Figures</b>	<b>xi</b>
<b>Chapter 1. Introduction</b>	<b>1</b>
<b>Chapter 2. Theoretical Foundations</b>	<b>3</b>
2.1 Nuclear Magnetic Resonance . . . . .	3
2.1.1 Equation of Motion of Isolated Spins in a Magnetic Field . . . . .	3
2.2 Bloch Equations . . . . .	5
2.3 Pulsed NMR . . . . .	8
2.3.1 Rotating Frame . . . . .	10
2.3.2 Measuring Relaxation in Pulsed NMR . . . . .	11
2.4 Magnetic Resonance Force Microscopy . . . . .	15
2.4.1 Force Detected Magnetic Resonance . . . . .	16
2.4.2 Cyclic Adiabatic Inversion of Magnetization . . . . .	16
2.4.3 Cantilever Dynamics . . . . .	20
2.4.4 Measuring $T_1$ and $T_2$ with MRFM . . . . .	24
2.4.5 Spin Nutation and Calibration of $B_1$ . . . . .	26
<b>Chapter 3. MRFM Instruments</b>	<b>28</b>
3.1 Cantilever . . . . .	28
3.1.1 Introduction to double torsional oscillators . . . . .	29
3.1.2 Fabrication . . . . .	30
3.1.3 Characterization . . . . .	35



3.1.4 Fiber Optic Interferometer . . . . .	39
3.2 RF components . . . . .	44
3.3 3-Axis Piezoelectric Positioners . . . . .	47
<b>Chapter 4. Experiments</b>	<b>52</b>
4.1 Magnetic Field Gradient . . . . .	52
4.2 Initial Attempt to Observe Force-detected MRFM . . . . .	55
4.3 Troubleshooting . . . . .	59
<b>Chapter 5. Future Directions</b>	<b>71</b>
5.1 Modifications to the Experimental Setup . . . . .	71
5.2 Phase Cycling . . . . .	72
<b>Appendices</b>	<b>76</b>
<b>Appendix A. Feedback Electronics</b>	<b>77</b>
<b>Appendix B. Inertial Positioner Driver Electronics</b>	<b>81</b>
<b>Appendix C. Frequency Modulation Electronics</b>	<b>88</b>
<b>Appendix D. Errata in Oxford’s HelioxVL <sup>3</sup>He Insert Manual</b>	<b>92</b>
<b>Bibliography</b>	<b>93</b>
<b>Index</b>	<b>100</b>
<b>Vita</b>	<b>101</b>

## List of Tables

## List of Figures

2.1	Spin-1/2 system in a magnetic field. The energy level degeneracy is lifted. . . . .	6
2.2	Relaxation of magnetization and the proportionality constant $T_1$ . . . . .	7
2.3	Illustration of an NMR experiment. A one-coil geometry is shown. In a one-coil geometry, the same coil used to apply RF pulses is used as the signal pickup coil. . . . .	9
2.4	Illustration of how time-varying RF field (bottom row) can be decomposed to two counter-rotating RF fields (top row). . . . .	10
2.5	Sequence for measuring $T_1$ . When the resonance condition is met, the effective field does not have a $z$ axis component (as shown in a) through c)). However, when the RF field is turned off, only the external field $\mathbf{B}_0$ is present (as shown in d) and f)). Therefore, the magnetization will relax toward the external field with the spin-lattice or longitudinal relaxation time $T_1$ . a) Application of $\pi$ -pulse. b) Magnetization rotating about the effective field. c) Magnetization rotated $90^\circ$ . d) RF turned off. The $z$ component of magnetization decays to $M_0$ . e) After some time $\tau$ , $\pi/2$ is applied. f) The magnetization is fully relaxed. . . . .	12
2.6	Illustration of how spins dephase in the transverse plane after the application of $\pi/2$ -pulse due to field inhomogeneity. . . . .	14
2.7	Effect of $\pi$ -pulse and formation of spin echo. a) Immediately after a $\pi/2$ -pulse. b) Evolution of spin isochromats for time $\tau$ . c) After application of a $\pi$ -pulse. Spins that were ahead and lagged behind will come together. d) Formation of spin echo for time $2\tau$ . e) Timing diagram for pulses. The echo will have a different sign from the FID (free induction decay) right after the $\pi/2$ -pulse. With an application of $\pi$ -pulse along the $y'$ axis, the echo will have the same sign as the FID. . . . .	14
2.8	Each $\pi$ -pulse refocuses dephased spin isochromats. The envelope of the decay is fitted to decaying exponential to extract $T_2$ . Each of refocused magnetization echos can be fitted to an exponential to obtain $T_2^*$ . From [46] . . . . .	15
2.9	Pictorial presentation of magnetic resonance force microscopy experiment. . . . .	17

2.10	Time evolution of effective field in the rotating frame. At any given time, the $z$ component of $B_{\text{eff}}$ is given by $\frac{\Omega}{\gamma} \sin(\omega_{\text{osc}})$ while the $x'$ component is always $B_1$ . . . . .	18
2.11	Illustration of cyclic adiabatic inversion. . . . .	19
2.12	RF pulse sequence used for measuring spin-lattice relaxation time $T_1$ . . . . .	24
2.13	RF pulse sequence used for measuring spin-spin relaxation time $T_2$ . . . . .	25
2.14	RF pulse sequence used for spin nutation experiment. . . . .	26
3.1	First four lowest normal modes of double torsional oscillators. For a description of each mode, see text. . . . .	29
3.2	Double torsional oscillator fabrication process . . . . .	31
3.3	Critical point drying using $\text{CO}_2$ . Point A: Micro-fabricated oscillators are in liquid $\text{CO}_2$ . Point B: The pressure vessel is closed and the temperature of the vessel is raised above the critical temperature of $\text{CO}_2$ , which is $31.1^\circ\text{C}$ . Since the pressure vessel is closed, the pressure rises with temperature. Once the temperature is above the critical temperature, the pressure will also be above the critical pressure. Point C: The pressure is released slowly to the atmosphere. The liquid-gas phase boundary has not been crossed, and micro-oscillators are successfully dried without experiencing the surface tension of the gas-liquid interface. . . . .	34
3.4	Configuration for driven scans for measuring resonant frequencies of oscillators. Red lines indicate optical signal paths, while blue lines indicate electrical signal paths. . . . .	36
3.5	An example of resonant frequency scan. Scans can be fitted to Lorentzian to extract the precise location of the peak and the quality factor of resonance . . . . .	37
3.6	Typical measurement results. a) Driven scan. b) Ring-down measurement used to determine the quality factor. c) PSD estimation by the modified Welch method. d) Integrated area under the curve in c). Red curves are fits to the data. . . . .	40
3.7	Fiber optic interferometer used in current setup. The photodiode is also sensitive for a $1550\text{ nm}$ laser. A $1550\text{ nm}$ laser will reduce heating of oscillators, but the overall sensitivity of displacement measurement decreases. . . . .	41

3.8	A typical interference fringe as a function of interferometer cavity length. The interferometer should be operated at the center of the fringe in order to use the linear approximation for small changes in signal. . . . .	43
3.9	RF tank circuit: series matched and parallel tuned circuit. . .	45
3.10	3-dimensional CAD view of 3-axis positioner. . . . .	48
3.11	Picture of both stages installed in the probe. The RF board containing RF circuitry and cantilever mount are not shown. .	49
3.12	Block diagram for the inertial positioner controller. Blue lines indicate digital signal paths, while red lines indicate analog signal paths. . . . .	50
4.1	Calculation of magnetic field from the fully saturated iron cylinder with dimensions given in the text. This field will need to be added to the field from the superconducting magnet in order to correctly calculate the resonant field. . . . .	53
4.2	Calculation of magnetic field gradient from the fully saturated iron cylinder with dimensions given in the text. Once the operating distance is determined, the resonant slice thickness can be estimated by (4.1). . . . .	54
4.3	Close-up picture showing components and their relative positions. The cantilever shown is 200 $\mu\text{m}$ long. The iron cylinder is normally placed within 1 mm from the sample. It has been backed up in order to not block the view of other components.	55
4.4	SEM image showing a sample attached at the end of a cantilever.	56
4.5	Block diagram showing various connections for the experiment. Green lines indicate optical signal paths, red lines indicate analog signal paths, and blue lines indicate digital signal paths. Orange boxed parts indicate homemade components. The positioner and its electronics for advancing and retracting the iron magnet and fiber are not shown in the diagram. . . . .	57
4.6	Typical single-sweep data and amplitude plot as a function of magnet-sample distance. . . . .	58
4.7	An example of a measured spin echo from a sample of $\text{D}_2\text{O}$ . It is measured with a millimeter-size coil. . . . .	62
4.8	$T_1$ measurement from the conventional NMR experiment with a millimeter-size coil. The standard saturation recovery with a $\pi/2 - \tau - \pi$ pulse sequence was used for measurement as discussed in Chapter 2. For a comparison of data, see result from [11]. The solid line is an exponential fit to the data. . . . .	63

4.9	Ringling in the ENI 5100L RF amplifier output. This ringling lasts for several tens of $\mu\text{s}$ . From [11]. We have observed the identical ringling. . . . .	65
4.10	Dependence of spurious excitation on RF input power. The ENI 5100L RF amplifier was used to obtain this result. Note the non-linearity as opposed to a linear behavior claimed by others [31, 33]. . . . .	67
5.1	Two-step phase cycling from [9]. . . . .	73
5.2	a) First of the two readout sequence in the two-step phase cycling. $B_{\text{eff}}$ and $M$ are aligned anti-parallel initially. See text for the explanation. The cyclic adiabatic inversion sequence with the $x$ -phase RF brings $B_{\text{eff}}$ onto the $x$ axis. The resulting $z$ components are graphically shown. b) Second of the two readout sequence. After the last $\pi/2$ -pulse, $M$ and $B_{\text{eff}}$ are aligned parallel. The cyclic adiabatic inversion sequence with the $-x$ -phase RF brings both $M$ and $B_{\text{eff}}$ onto $-x$ axis. The resulting $z$ components are graphically shown. . . . .	74
A.1	Interferometer feedback circuit. . . . .	78
B.1	75 V power supply using a TL783 linear regulator from Texas Instruments. Proper heat sinking is required for stable operation. For more information, refer to the datasheet for the TL783 from Texas Instruments. . . . .	82
B.2	Low Voltage Power Supplies. The design can be used in any laboratory DC power application. Proper heat sinking is required for regulators. . . . .	84
B.3	DAC Connection diagram to PIC micro-controller. . . . .	85
B.4	Sawtooth waveform controls. . . . .	86
C.1	Frequency modulation electronics responsible for correctly timing signal generator. . . . .	89
C.2	An example of FM voltage signal generation. a) Triangular FM voltage used in MRFM. b) Two components of FM voltage. c) Waveform output in synchrony with TTL output . . . . .	91

# Chapter 1

## Introduction

Magnetic resonance force microscopy (MRFM) was first proposed in 1991 [39] by John Sidles as one possible mean to determine 3-dimensional structures of proteins. Since the first experimental demonstration in 1992 in which an electron spin resonance signal [38] was observed, several groups have pursued single nuclear spin sensitivity. So far, Dan Rugar of IBM has been able to detect a signal from one electron spin [36]. However, the detection efficiency was severely hampered by long averaging times,  $\sim 13$  hours per data point [36]. Also, the sample was prepared in a controlled way such that the unpaired electrons were largely separated. Since a nuclear moment is about 1000 times smaller than that of an electron, single nuclear spin sensitivity is out of reach with current technology. However, there are several ways to improve the sensitivity needed for a successful single nuclear spin imaging experiment. The minimum detectable force,  $F_{\min}$ , is given by [45]

$$F_{\min} = \sqrt{\frac{4kk_B T \Delta\nu}{Q\omega_{\text{osc}}}} \quad (1.1)$$

As the above equation shows, one can improve the sensitivity of a MRFM instruments in several ways. The mechanical detector, in this case a cantilever or an oscillator, can be made to have a small spring constant,  $k$ , a large quality

factor,  $Q$ , and a large resonant frequency,  $\omega_{\text{osc}}$ . Also, lowering the operating temperature contributes to a better signal to noise ratio. Jenkins et al. [21] have fabricated cantilevers with spring constants as small as  $10^{-5}$  N/m. Experimental applications of ultra-soft cantilevers to MRFM at liquid helium temperature have been successful [16, 29, 44, 47, 49]. In particular, Mamin and Rugar have achieved the sub-atto-Newton force sensitivity by operating their microscope at milli-kelvin temperatures. The sensitivity of the MRFM probe has been doubled every six months on average since 1992. This remarkable statement is somewhat akin to Moore's law in the semiconductor industry. This dissertation is structured to introduce the basic theoretical foundations and to describe our own efforts in the construction of a versatile, low temperature nuclear MRFM (NMRFM) probe.



## Chapter 2

### Theoretical Foundations

#### 2.1 Nuclear Magnetic Resonance

Nuclear magnetic resonance is a physical phenomenon because of nuclear magnetism. Not all nuclei are NMR active. In a typical NMR experiment, a nuclear magnetic moment is aligned to an external field,  $\mathbf{B}_0$ , and this alignment is perturbed by an electromagnetic field, which is typically in the radio frequency range. The response to this perturbation is exploited in various imaging and spectroscopic NMR experiments. Although a thorough quantum mechanical treatment of NMR can be given, a semi-classical model where magnetic moments are treated vectorially provides a description much easier to understand. For simplicity, only spin 1/2 nuclei such as hydrogen, fluorine, phosphorus, etc. will be discussed.

##### 2.1.1 Equation of Motion of Isolated Spins in a Magnetic Field

A nucleus can possess a total magnetic moment,  $\boldsymbol{\mu}$ , and a total angular momentum,  $\mathbf{J}$ , because it could consist of many particles. The gyromagnetic

ratio  $\gamma$  that relates both quantities is defined as

$$\boldsymbol{\mu} = \gamma \mathbf{J} \quad (2.1)$$

From quantum mechanics, we know that the total angular momentum is defined by

$$\mathbf{J} = \hbar \mathbf{I} \quad (2.2)$$

where  $\mathbf{I}$  is the dimensionless angular momentum operator. We know that  $\mathbf{I}_z$ , the  $z$  axis component of the angular momentum, and  $\mathbf{I}^2$  commute so that their eigenvalues can be obtained simultaneously. If  $I$  is the quantum number such that the eigenvalue of  $\mathbf{I}^2$  is  $I(I + 1)$ , then the eigenvalue of  $\mathbf{I}_z$ , denoted by  $m$ , can take any of  $2I + 1$  values  $-I, -I + 1, \dots, I - 1, I$ .

When a magnetic moment is placed in a magnetic field,  $\mathbf{B}$ , the interaction Hamiltonian is given by

$$\mathcal{H} = -\boldsymbol{\mu} \cdot \mathbf{B} \quad (2.3)$$

If we arbitrarily choose the direction of  $\mathbf{B}$  to be along the  $z$  axis, the Hamiltonian can be simplified and the eigenvalues of the Hamiltonian can be calculated

$$\mathcal{H} = -\gamma \hbar B_0 I_z \quad (2.4a)$$

$$E = -\gamma \hbar B_0 m \quad m = I, I - 1, \dots, -I + 1, -I \quad (2.4b)$$

For a spin  $1/2$  particle,  $m$  can be  $1/2$  or  $-1/2$ . This means that there are only two discrete energy levels and their degeneracy is removed by the application of a magnetic field. The energy level difference is given by

$$\Delta E = \gamma \hbar B_0 = \hbar \omega_0 \quad (2.5)$$

Hence, we can induce a transition when the resonance condition,  $\omega_0 = \gamma B_0$ , is satisfied. In an NMR experiment, the energy of the photons falls typically in the radiofrequency range ( $\sim$  MHz) of the electromagnetic spectrum.

When a magnetic moment  $\boldsymbol{\mu}$  is placed in a magnetic field,  $\mathbf{B}$ , the equation of motion is given by

$$\boldsymbol{\tau} = \frac{d\mathbf{J}}{dt} = \boldsymbol{\mu} \times \mathbf{B} \quad (2.6a)$$

$$\frac{d\boldsymbol{\mu}}{dt} = \boldsymbol{\mu} \times (\gamma \mathbf{B}) \quad (2.6b)$$

Similarly for the net magnetization,  $\mathbf{M}$ , the same equation of motion holds.

$$\frac{d\mathbf{M}}{dt} = \mathbf{M} \times (\gamma \mathbf{B}) \quad (2.7)$$

## 2.2 Bloch Equations

If  $\mathbf{B} = B_0 \hat{\mathbf{k}}$  and the the spins have reached an equilibrium with temperature  $T$ , the components of the net magnetization are

$$M_x = M_y = 0 \quad (2.8a)$$

$$M_z = M_0 = \frac{\chi_0}{\mu_0} B_0 = \frac{CB_0}{T} \quad (2.8b)$$

where  $C$  is the Curie constant. If we assume that the number of spin-up and spin-down nuclei are  $N_\uparrow$  and  $N_\downarrow$  respectively, the following holds

$$M_z = \mu(N_\uparrow - N_\downarrow) \quad (2.9)$$

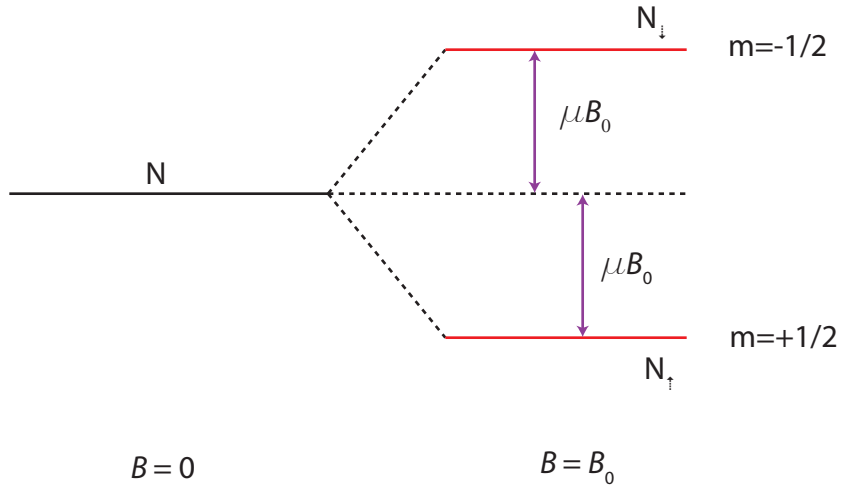


Figure 2.1: Spin-1/2 system in a magnetic field. The energy level degeneracy is lifted.

At a finite temperature  $T$ , the population of spin-up and spin-down states is described by the Boltzmann distribution

$$\frac{N_{\uparrow}}{N_{\downarrow}} = \exp(-2\mu B_0/k_B T) \quad (2.10)$$

Solving (2.9) and (2.10), it can be shown

$$M_0 = N\mu \tanh(\mu B_0/k_B T) \quad (2.11)$$

where  $N = N_{\uparrow} + N_{\downarrow}$ . The result (2.11) describes the net magnetization after an equilibrium has been reached. However, the magnetization does not grow instantly to  $M_0$  after the application of  $B_0$ . Rather, the magnetization usually grows to  $M_0$  with some time constant at a rate proportional to the difference from equilibrium. Thus we can write

$$\frac{dM_z(t)}{dt} \propto M_0 - M_z(t) \quad (2.12)$$

where  $M_z(t)$  is the magnetization at time  $t$ . When we take  $T_1$  as the time constant that satisfy above proportionality, we can claim the following equations are obtained.

$$\frac{dM_z(t)}{dt} = \frac{M_0 - M_z(t)}{T_1} \quad (2.13a)$$

$$M_z = M_0(1 - e^{-t/T_1}) \quad (2.13b)$$

(2.13b) can be graphically understood as in Figure 2.2. Since the energy of

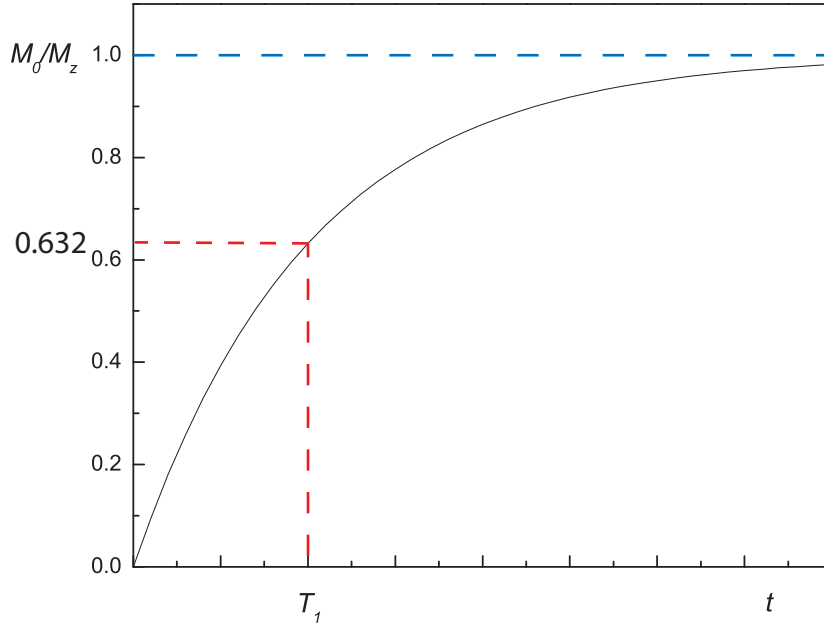


Figure 2.2: Relaxation of magnetization and the proportionality constant  $T_1$ .

the magnetization is given by  $-\mathbf{M} \cdot \mathbf{B}$ , the energy decreases to the equilibrium value  $-M_0 B_0$  as  $t \rightarrow \infty$ . The energy dissipated in this process is transferred to some other reservoir of energy, and ultimately to the lattice as heat. Thus, the time constant  $T_1$  is called the spin-lattice relaxation time. Since the energy change involves changing component of  $M$  along the magnetic field, it is also

know as the longitudinal relaxation time. When  $T_1$  is short, the magnetization can easily exchange energy with the lattice, while long spin-lattice relaxation time means the opposite.

More generally magnetization has  $M_x$  and  $M_y$  components, in addition to  $M_z$ . Therefore, the equations that describe the evolution of the magnetization can be written more completely as

$$\frac{dM_z}{dt} = \gamma(\mathbf{M} \times \mathbf{B})_z + \frac{M_0 - M_z}{T_1} \quad (2.14a)$$

$$\frac{dM_x}{dt} = \gamma(\mathbf{M} \times \mathbf{B})_x + \frac{M_x}{T_2} \quad (2.14b)$$

$$\frac{dM_y}{dt} = \gamma(\mathbf{M} \times \mathbf{B})_y + \frac{M_y}{T_2} \quad (2.14c)$$

These equations are called Bloch's phenomenological equations. Note that  $T_2$  is the relaxation time in  $x$ - $y$  plane, perpendicular to the external field  $\mathbf{B}$ .  $T_2$  is called the transverse relaxation or spin-spin relaxation time.

## 2.3 Pulsed NMR

In this section, how one can measure  $T_1$  and  $T_2$  in a pulsed NMR experiment is described. In the subsequent section, how  $T_1$  and  $T_2$  are measured in an NMRFM experiment will be presented for comparison.

Figure 2.3 shows a generic one-coil NMR setup. The external field  $\mathbf{B}$  is several tesla in strength.<sup>1</sup> The sample lies in the solenoid, and the external field  $\mathbf{B}$  is aligned perpendicular to the axis of the solenoid, say the  $z$  axis.

---

<sup>1</sup>For example,  $\mathbf{B}$  is 7.0456 T for a 300 MHz proton NMR spectrometer.

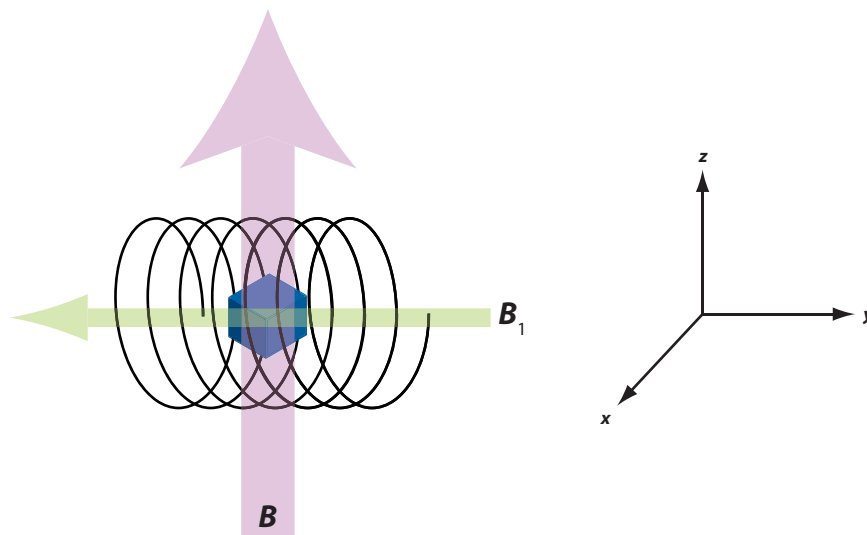


Figure 2.3: Illustration of an NMR experiment. A one-coil geometry is shown. In a one-coil geometry, the same coil used to apply RF pulses is used as the signal pickup coil.

If, instead of  $B$ ,  $B_1$  is applied in the  $y$  axis direction, the magnetization will start to precess around  $B_1$ , meaning it will move in the  $x$ - $z$  plane. Hence, by controlling the duration of RF exposure, the magnetization can be rotated to any angle. But the external field  $B$  is usually provided by a superconducting solenoid magnet, and the field cannot be turned off instantly, and  $B_1$  is on the order of 10 to 20 gauss<sup>2</sup> which is much smaller than  $B$ . Then how can one tilt the magnetization away from  $z$  axis? The answer is to exploit the resonance phenomenon.

---

<sup>2</sup>for solid state NMR

### 2.3.1 Rotating Frame

Suppose a time-varying RF field  $\mathbf{B}_1$  with frequency  $\omega_{\text{rf}}$  is applied perpendicular to the external field, say along the  $y$  axis. This field can be decomposed into two counter-rotating fields in the  $x$ - $y$  plane with the same frequency  $\omega_{\text{rf}}$ . This is pictorially shown in Figure 2.4. If we write the sinusoidally varying

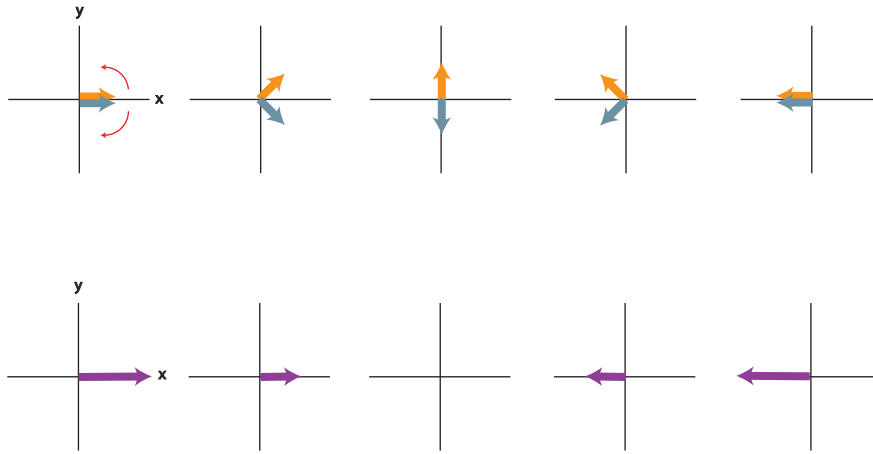


Figure 2.4: Illustration of how time-varying RF field (bottom row) can be decomposed to two counter-rotating RF fields (top row).

field in the  $x$  axis to be

$$\mathbf{B}_1 = 2B_1 \cos(\omega_{\text{rf}}t) \hat{\mathbf{x}} \quad (2.15)$$

then we can rewrite that as

$$\mathbf{B}_1 = [\cos(\omega_{\text{rf}}t) + \cos(-\omega_{\text{rf}}t)] \hat{\mathbf{x}} + [\sin(\omega_{\text{rf}}t) + \sin(-\omega_{\text{rf}}t)] \hat{\mathbf{y}} \quad (2.16)$$

After a coordinate transformation to which the new reference frame is rotating with the frequency  $\omega_{\text{rf}}$ ,<sup>3</sup> the equation of motion in the rotating frame can be

---

<sup>3</sup>For a complete mathematical derivation, see [40].



written as

$$\frac{d\mathbf{M}}{dt} = \gamma\mathbf{M} \times \left[ \left( B_0 - \frac{\omega_{\text{rf}}}{\gamma} \right) \hat{z} + B_1 \hat{x}' \right] \quad (2.17)$$

where  $x'$  denotes the rotating  $x$  axis. The term in the bracket is called the effective field. Here we see that when  $\omega_{\text{rf}} = \omega_0$ , the  $z$  component of the effective field vanishes. Since the  $z$  axis remains unchanged under the coordinate transformation,<sup>4</sup> there is no effective magnetic field component in the  $z$  direction in the laboratory frame. The condition  $\omega_{\text{rf}} = \omega_0$  is called the resonance condition. When such a condition is met, the magnetization will start to precess about the  $x'$  axis. By controlling the strength of  $B_1$  and the duration of its application, the magnetization will rotate about that  $x'$  axis. The angle of rotation  $\theta$  is mathematically written in terms of the pulse duration  $t$  as

$$\theta = \gamma B_1 t \quad (2.18)$$

When  $\theta = \frac{\pi}{2}$ , such a pulse is called a  $\frac{\pi}{2}$ -pulse. Similarly, When  $\theta = \pi$ , it is called a  $\pi$ -pulse.

### 2.3.2 Measuring Relaxation in Pulsed NMR

After the sample magnetization is tipped  $180^\circ$  say about the  $-x'$  axis, it will be along the  $-z$  axis. In the presence of external field only, it will relax back to the  $z$  axis with the characteristic time  $T_1$ . A popular pulse sequence for measuring  $T_1$  is pictorially shown in Figure 2.5. The basic pulse sequence pattern is called  $\pi - \tau - \pi/2$ . This means first a  $\pi$ -pulse is used to invert the

---

<sup>4</sup>In other words,  $z$  axis is the same for both laboratory and rotating frames

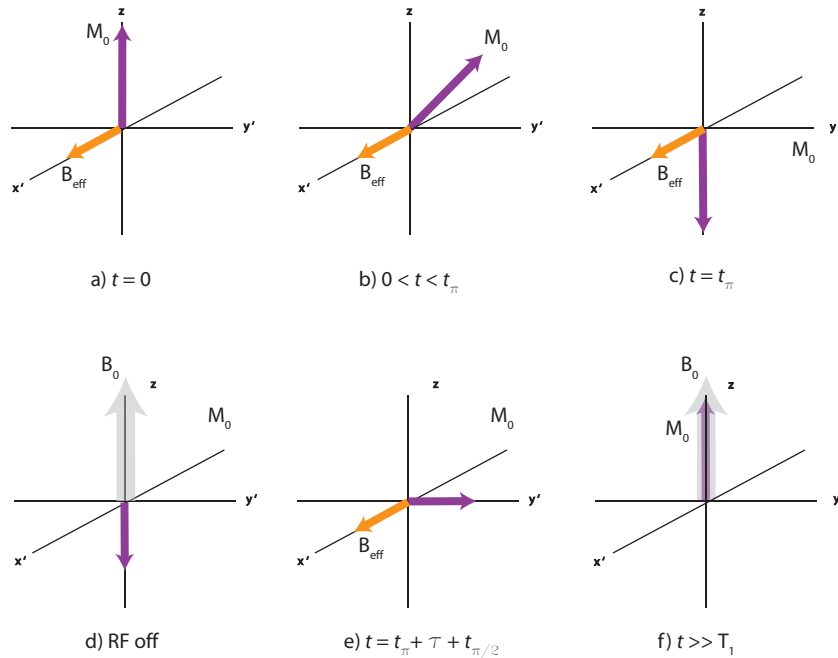


Figure 2.5: Sequence for measuring  $T_1$ . When the resonance condition is met, the effective field does not have a  $z$  axis component (as shown in a) through c)). However, when the RF field is turned off, only the external field  $\mathbf{B}_0$  is present (as shown in d) and f)). Therefore, the magnetization will relax toward the external field with the spin-lattice or longitudinal relaxation time  $T_1$ . a) Application of  $\pi$ -pulse. b) Magnetization rotating about the effective field. c) Magnetization rotated  $90^\circ$ . d) RF turned off. The  $z$  component of magnetization decays to  $M_0$ . e) After some time  $\tau$ ,  $\pi/2$  is applied. f) The magnetization is fully relaxed.

magnetization. Then the magnetization is allowed to relax for time  $\tau$ . As one waits after the  $\pi$ -pulse, the  $z$  component of the magnetization will go from  $-M_0$  to  $M_0$ . A  $\pi/2$ -pulse is used to place the partially relaxed magnetization in the  $x'$ - $y'$  plane so that the pickup coil can measure the remaining magnetization. The time evolution of the  $z$  component of the magnetization is given by

$$M(t) = M_0(1 - 2e^{-t/T_1}) \quad (2.19)$$

In practice, the magnetization may not be perfectly inverted, so the  $T_1$  recovery curve must be fit to  $M(t) = M_0(1 - Ae^{-t/T_1})$  where  $A \leq 2$ .

For measuring  $T_2$ , the spin-spin relaxation time or transverse relaxation time, we need to look at the time evolution of the magnetization in detail after a  $\pi/2$ -pulse. Shortly after a  $\pi/2$ -pulse say along the  $x'$  axis, the magnetization will be along the  $y'$  axis initially. If there was no field inhomogeneity, spins in the entire sample will precess about the external field with only one precessional frequency. However, there exists a certain degree of field inhomogeneity in a real experiment. Therefore, spins in different parts will precess with different precessional frequencies. Spins experiencing a higher field will precess faster than those experiencing a lower field. The magnetization in the  $x'$ - $y'$  plane will eventually dephase with the time constant  $T_2^*$ . This situation is described in Figure 2.6. The concept of spin echo is introduced next. After a  $\pi/2$ -pulse, a  $\pi$ -pulse is applied in the  $x'$  axis after a time delay of  $\tau$ . The situation is illustrated in Figure 2.7. In order to measure only  $T_2$ , the effect of field inhomogeneity must be removed. Figure 2.8 shows a procedure for RF pulses to measure  $T_2$ .

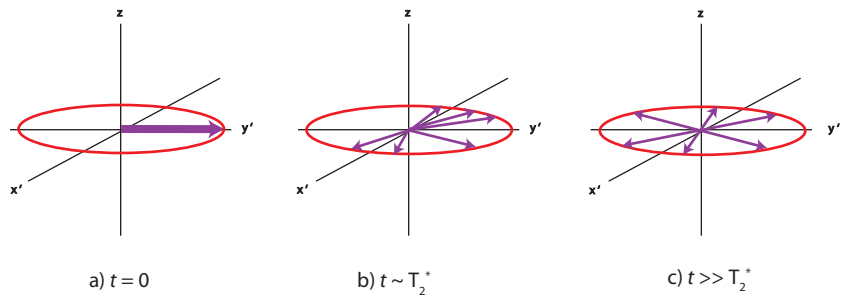


Figure 2.6: Illustration of how spins dephase in the transverse plane after the application of  $\pi/2$ -pulse due to field inhomogeneity.

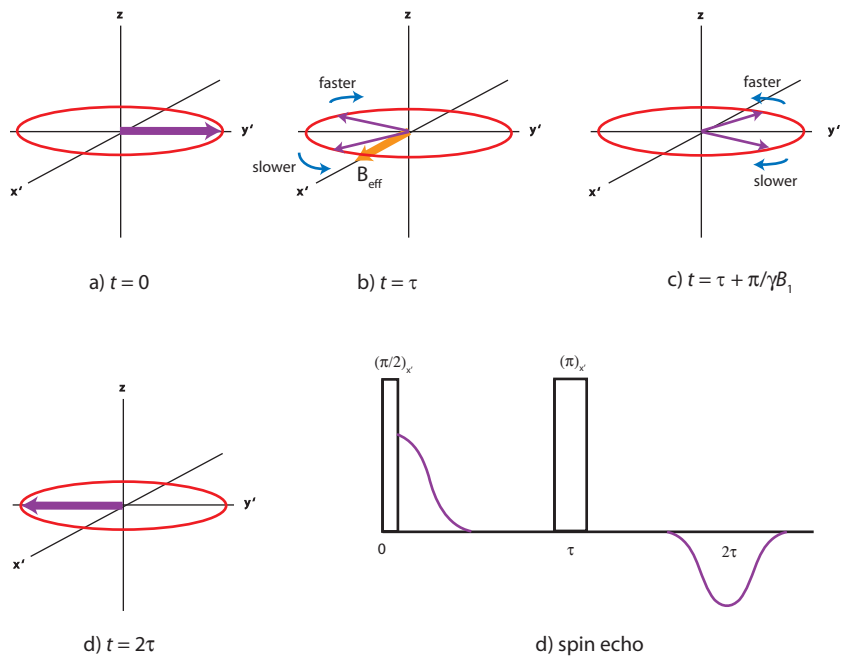


Figure 2.7: Effect of  $\pi$ -pulse and formation of spin echo. a) Immediately after a  $\pi/2$ -pulse. b) Evolution of spin isochromats for time  $\tau$ . c) After application of a  $\pi$ -pulse. Spins that were ahead and lagged behind will come together. d) Formation of spin echo for time  $2\tau$ . e) Timing diagram for pulses. The echo will have a different sign from the FID (free induction decay) right after the  $\pi/2$ -pulse. With an application of  $\pi$ -pulse along the  $y'$  axis, the echo will have the same sign as the FID.

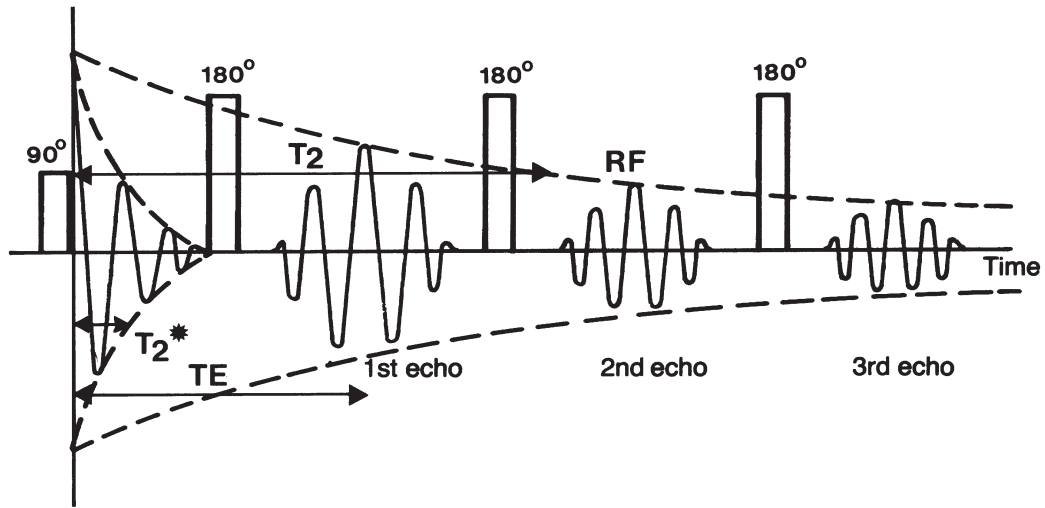


Figure 2.8: Each  $\pi$ -pulse refocuses dephased spin isochromats. The envelope of the decay is fitted to decaying exponential to extract  $T_2$ . Each of refocused magnetization echos can be fitted to an exponential to obtain  $T_2^*$ . From [46]

## 2.4 Magnetic Resonance Force Microscopy

Magnetic resonance force microscopy is a newly emerging technique that derives much of the technique from already well established magnetic resonance microscopy such as NMR and ESR (electron spin resonance). The major difference between the two techniques is in the detection method: mechanical detection for force microscopy and inductive detection for traditional magnetic resonance microscopy. In the subsequent sections, how magnetic resonance and relaxation time constants can be force-detected will be discussed.

### 2.4.1 Force Detected Magnetic Resonance

In an MRFM experiment, a sample magnetization is coupled to a mechanical oscillator or cantilever<sup>5</sup> through a gradient-producing magnet. The interaction between the gradient magnet and the sample is given by

$$\mathbf{F} = (\mathbf{M} \cdot \nabla)\mathbf{B} \quad (2.20)$$

For a one-dimensional experiment, say with the static field and the equilibrium magnetization along the  $z$  axis, (2.20) can be written as

$$F_z(t) = M_z \frac{\partial B}{\partial z} \quad (2.21)$$

In order to induce a time-dependent interaction, either  $M_z$  or  $B_z$  or both of them must be made time dependent. Since changing the magnetic field is not convenient, the  $z$  component of the sample magnetization is made time dependent using conventional magnetic resonance techniques with RF pulses.

### 2.4.2 Cyclic Adiabatic Inversion of Magnetization

Cyclic adiabatic inversion is an extension of adiabatic fast passage[13]. From (2.17), if we modulate the frequency of the radiofrequency field as  $\omega_{\text{rf}} = \omega_0 + \Omega \sin(\omega_{\text{osc}}t)$ , we can rewrite the effective field in the following form:

$$\begin{aligned} \mathbf{B}_{\text{eff}} &= \left( B_0 - \frac{\omega_0}{\gamma} - \frac{\Omega}{\gamma} \sin(\omega_{\text{osc}}t) \right) \hat{\mathbf{z}} + B_1 \hat{\mathbf{x}}' \\ &= \left( -\frac{\Omega}{\gamma} \sin(\omega_{\text{osc}}t) \right) \hat{\mathbf{z}} + B_1 \hat{\mathbf{x}}' \end{aligned} \quad (2.22)$$

---

<sup>5</sup>such as ones used in atomic force microscopy. However, the spring constants of oscillators (typically  $10^{-2}$  N/m or smaller) used in MRFM are much smaller than those of typical tapping mode cantilevers (tens to hundreds N/m).

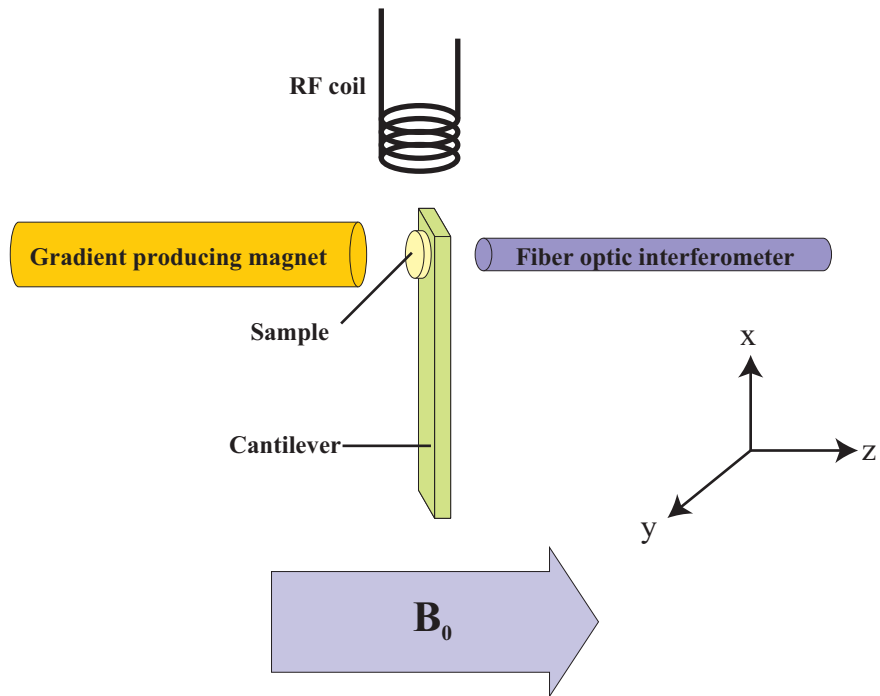


Figure 2.9: Pictorial presentation of magnetic resonance force microscopy experiment.

where  $\omega_{\text{osc}}$  is the resonant frequency of a mechanical oscillator. The situation is graphically represented in Figure 2.10. By starting the frequency modulation from far away from the resonance, meaning large  $\omega/\gamma$ , compared to  $B_1$ , the effective field starts very close to the external field in the  $z$  direction. This effective field must change slowly enough for the magnetization to follow. If the change is not slow enough, the magnetization will not truly lock onto

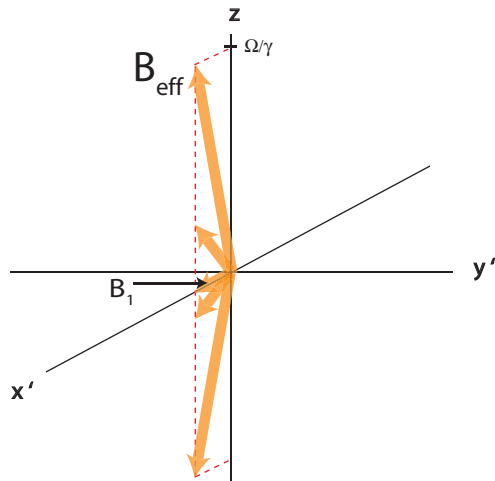


Figure 2.10: Time evolution of effective field in the rotating frame. At any given time, the  $z$  component of  $B_{\text{eff}}$  is given by  $\frac{\Omega}{\gamma} \sin(\omega_{\text{osc}})$  while the  $x'$  component is always  $B_1$ .

the effective field during the fast passage. This adiabatic condition<sup>6</sup> for a triangular modulation is given in [15] as

$$\Omega \ll \frac{\gamma^2 B_1^2}{4f_{\text{osc}}} \quad (2.23)$$

Experiments have found that the term on the right side of (2.23) should be at least 2 to 3 times larger than  $\Omega$  in order not to violate the adiabatic condition.

In an MRFM experiment, this spin-locking technique is used for samples with  $T_1$  greater than the mechanical resonant frequency of an oscillator used. As shown in Figure 2.11, after approaching the magnetic resonance

---

<sup>6</sup>For a more complete discussion of adiabatic conditions, see [33].



from far below, the effective field is adiabatically and cyclically modulated at  $\omega_{\text{osc}}$  with a predetermined modulation depth. The reason for choosing the

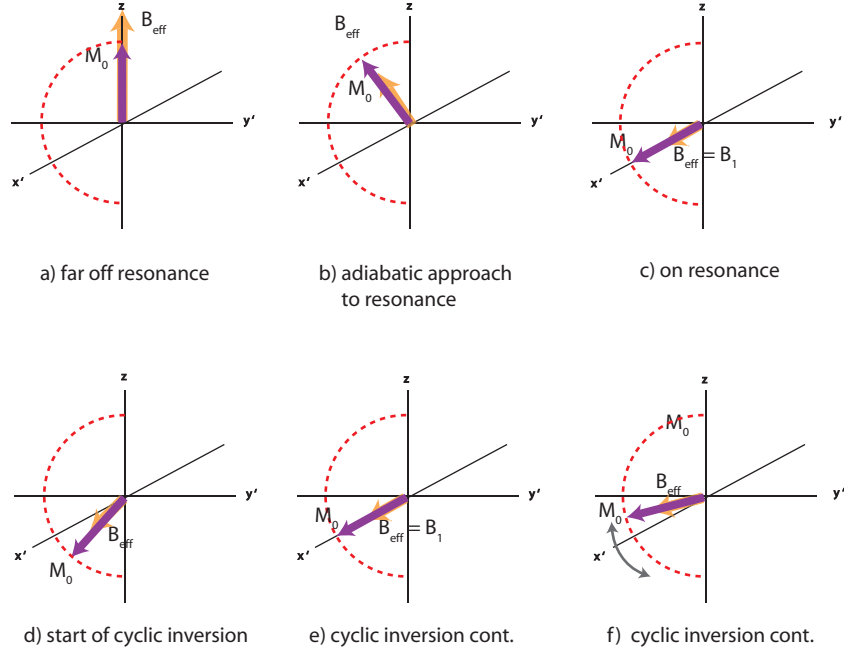


Figure 2.11: Illustration of cyclic adiabatic inversion.

modulation frequency to be  $\omega_{\text{osc}}$  is to exploit the mechanical resonance. At resonance, the amplitude of motion for a damped, driven harmonic oscillator is enhanced by the quantity called the quality factor  $Q$ . For oscillators or cantilevers made from single crystal silicon, the quality factor can be as high as  $\approx 10^6$  or more. Therefore, this amplification phenomena can be effectively utilized in detecting a very small force. We now digress and discuss cantilever dynamics in detail because the oscillator used as the force detector is modeled as a damped, driven oscillator.

### 2.4.3 Cantilever Dynamics

Just as many physical phenomena can be approximated by simple harmonic motion or some variations on that, the cantilever driven by the spin-magnet interaction is well described by one-dimensional damped, driven harmonic oscillator. Because the amplitude of the motion induced by the interaction is small, the approximation for the cantilever motion as a damped, driven harmonic oscillator is valid.

The equation of motion for a damped, driven harmonic oscillator is given by

$$m \frac{d^2x}{dt^2} + \Gamma \frac{dx}{dt} + kx = F_0 \cos(\omega t) \quad (2.24)$$

The general solution to the above equation is given as the sum of the transient and the steady state solutions. The transient solution is the solution to damped, undriven simple harmonic oscillation that depends on the initial conditions. The steady state solution, however, does not depend on the initial conditions but on the amplitude and frequency of the driving force, the damping constant, etc. There are various classical mechanics textbooks that discuss the harmonic oscillation and its extensions to damped and driven cases [2, 27, 30].

First, the transient solution is found to be

$$x = c_1 \exp \left\{ -\frac{\Gamma t}{2m} + \left[ \sqrt{\left(\frac{\Gamma}{2m}\right)^2 - \frac{k}{m}} \right] t \right\} + c_2 \exp \left\{ -\frac{\Gamma t}{2m} - \left[ \sqrt{\left(\frac{\Gamma}{2m}\right)^2 - \frac{k}{m}} \right] t \right\} \quad (2.25)$$

Constants  $c_1$  and  $c_2$  are determined from the initial conditions. Knowing  $\omega_0 = \sqrt{k/m}$  and  $Q = m\omega_0/\Gamma$ , the transient solution can be written as

$$x = \exp\left(-\frac{\omega_0}{2Q}t\right) \left\{ c_1 \exp\left[\sqrt{\left(\frac{\omega_0}{2Q}\right)^2 - \omega_0^2} t\right] + c_2 \exp\left[-\sqrt{\left(\frac{\omega_0}{2Q}\right)^2 - \omega_0^2} t\right] \right\} \quad (2.26)$$

In a typical MRFM experiment, the quality factor,  $Q$ , is much bigger than unity. This is the under-damped case for a damped, driven harmonic oscillation. Therefore, the term inside the square root is negative, and the equation can be written as

$$x = \exp\left(-\frac{\omega_0}{2Q}t\right) [c_1 \exp(-i\omega_1 t) + c_2 \exp(i\omega_1 t)] \quad (2.27)$$

where  $\omega_1 = \omega_0 \sqrt{1 - (1/2Q)^2}$ . In general the coefficients  $c_1$  and  $c_2$  are complex, but if we adopt real constants such that

$$c'_1 \equiv c_1 + c_2, \quad c'_2 \equiv i(c_1 - c_2). \quad (2.28)$$

With Euler's relation  $e^{i\theta} = \cos \theta + i \sin \theta$ , the solution can be rewritten as

$$x = \exp\left(-\frac{\omega_0}{2Q}t\right) [c'_1 \cos(\omega_1 t) + c'_2 \sin(\omega_1 t)] \quad (2.29)$$

The solution implies that the sinusoidal oscillation amplitude will exponentially decay with the characteristic time constant of  $2Q/\omega_0$ . Hence, a large  $Q$  implies that the time constant will be large, and one must wait a correspondingly long time after a change in the system occurred to reach steady state.

The steady state solution is what must be measured in MRFM in order

to quantitatively extract the strength of interaction. The solution for the case of arbitrary driven force  $f(t)$  can be easily obtained using Fourier transform method. The differential equation to solve is given by

$$m \frac{d^2 x}{dt^2} + \Gamma \frac{dx}{dt} + kx = f(t) \quad (2.30)$$

Define Fourier transform pairs  $f(t)$  and  $F(\omega)$  and  $x(t)$  and  $\chi(\omega)$  as shown below.

$$f(t) = \int_{-\infty}^{\infty} F(\omega) e^{-i\omega t} d\omega \quad (2.31a)$$

$$F(\omega) = \frac{1}{2\pi} \int_{-\infty}^{\infty} f(t') e^{i\omega t'} dt' \quad (2.31b)$$

$$x(t) = \int_{-\infty}^{\infty} \chi(\omega) e^{-i\omega t} d\omega \quad (2.32a)$$

$$\chi(\omega) = \frac{1}{2\pi} \int_{-\infty}^{\infty} x(t') e^{i\omega t'} dt' \quad (2.32b)$$

After multiplying both sides by  $1/\sqrt{2\pi} \exp(i\omega t') dt'$  and integrating, one obtain

$$(-m\omega^2 - i\Gamma\omega + k)\chi(\omega) = F(\omega) \quad (2.33a)$$

$$\chi(\omega) = \frac{F(\omega)}{k - m\omega^2 - i\Gamma\omega} \quad (2.33b)$$

Performing an inverse Fourier transform, the steady state solution is obtained.

$$x(t) = \int_{-\infty}^{\infty} \frac{F(\omega) e^{-i\omega t} d\omega}{k - m\omega^2 - i\Gamma\omega} \quad (2.34)$$

At this point, unless we are given more specific information about  $f(t)$ , we cannot proceed further. Because the frequency modulation that induces a

time-dependent interaction force in MRFM is generally sinusoidal, we can assume that  $f(t) = F_0 \cos(\omega't)$  for  $t \geq 0$  and  $f(t) = 0$  for  $t < 0$ . There have been cases where different waveforms have been used such as sawtooth<sup>7</sup> and triangular modulations[15]. However, the analysis is similar in that any periodic waveforms can be Fourier decomposed. For convenience use the complex exponential  $e^{i\omega't}$  and take the real part of the result as the solution. Substituting the Fourier transform of assumed  $f(t)$  in Eq. (2.13), we obtain

$$x(t) = \int_{-\infty}^{\infty} \frac{F_0 i}{2\pi(\omega - \omega')} \frac{e^{-i\omega t} d\omega}{-m \left(\omega - \omega_0 + \frac{i\Gamma}{2m}\right) \left(\omega - \omega_0 - \frac{i\Gamma}{2m}\right)} \quad (2.35)$$

By calculating the residues it can be shown that the value of the integral is

$$\begin{aligned} x(t) &= -\frac{F_0}{m} \frac{e^{-i\omega't}}{(\omega' - \omega_0 + (i\Gamma/2m))(\omega' - \omega_0 + (i\Gamma/2m))} \\ &= -\frac{F_0}{m} \frac{e^{-i\omega't}(\omega'^2 - \omega_0^2 - (i\Gamma/m)\omega')}{(\omega'^2 - \omega_0^2)^2 + (\Gamma^2\omega'^2/m^2)} \end{aligned} \quad (2.36)$$

The real part of the result is the physically meaningful solution. Hence, the steady state solution is given by

$$x(t) = \frac{F_0}{m} \frac{(-\omega'^2 + \omega_0^2) \cos(\omega't) + (\Gamma/m)\omega' \sin(\omega't)}{(\omega'^2 - \omega_0^2)^2 + (\Gamma^2\omega'^2/m^2)} \quad (2.37)$$

By letting

$$C = (k/m - \omega'^2)^2 + (R\omega'/m)^2 \quad (2.38a)$$

$$\cos \phi = \frac{k/m - \omega'^2}{\sqrt{C}} \quad (2.38b)$$

$$\sin \phi = \frac{(R\omega'/m)}{\sqrt{C}} \quad (2.38c)$$

---

<sup>7</sup>D. Smith, private communication

the steady state solution can be rewritten as

$$x(t) = \frac{F_0}{m\sqrt{C}} \cos(\omega t - \phi) \quad (2.39)$$

Therefore, it can be seen that at resonance,  $\phi = \pi/2$ , and the steady state solution will be a sinusoid  $90^\circ$  out of phase with the driving force.

#### 2.4.4 Measuring $T_1$ and $T_2$ with MRFM

Figure 2.12 shows the RF pulse sequence for measuring  $T_1$ . First, the

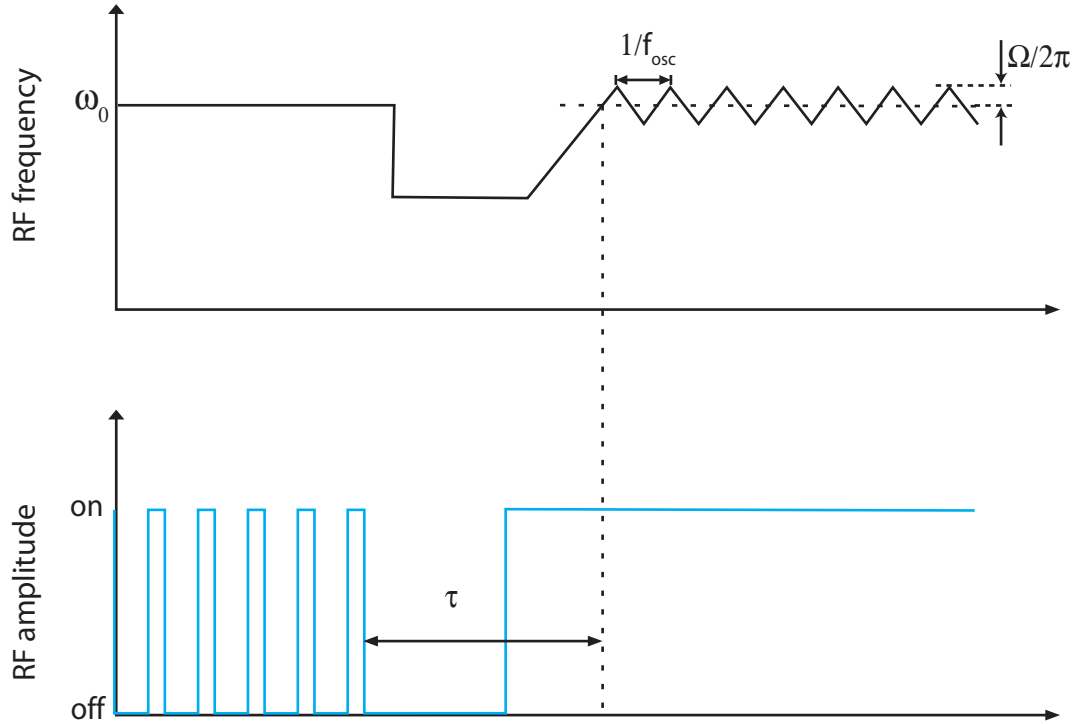


Figure 2.12: RF pulse sequence used for measuring spin-lattice relaxation time  $T_1$ .

magnetization  $M_0$  is destroyed with a saturation comb of  $\pi/2$ -pulses. Then,

the RF carrier frequency is moved to far below resonance before the start of the cyclic adiabatic inversion sequence while waiting some time  $\tau$  to allow the magnetization to recover. After waiting some time  $\tau$ , the cyclic adiabatic inversion sequence is carried out to read out how much of the magnetization has recovered. The resulting  $M_z(\tau)$  is described by

$$M_z(\tau) = M_0 (1 - e^{-\tau/T_1}) \quad (2.40)$$

Measuring  $T_2$  is by far the most time consuming relaxation time measurement in MRFM. Figure 2.13 illustrate the RF pulse sequence for measuring

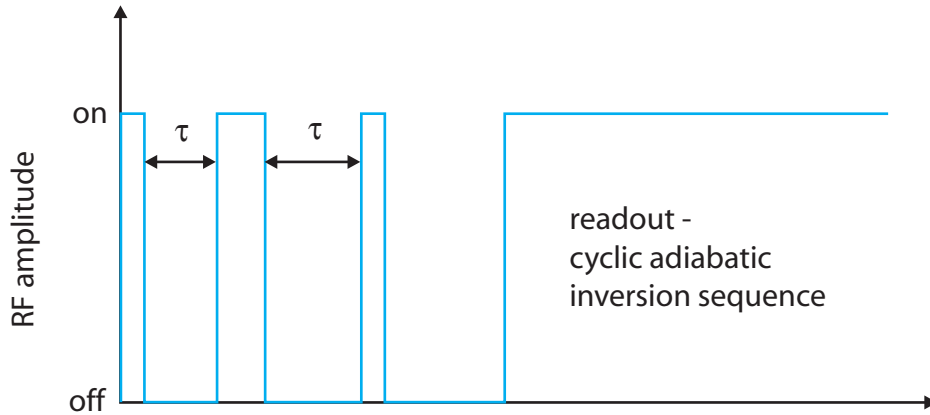


Figure 2.13: RF pulse sequence used for measuring spin-spin relaxation time  $T_2$ .

$T_2$ . First a  $\pi/2$ -pulse is applied to tip the magnetization  $M_0$  into  $x'-y'$  axis. Then some time  $\tau$  later a  $\pi$ -pulse is applied to refocus partially dephased magnetization. In a conventional NMR, one just needs to watch the magnetization coming into focus, but in MRFM we must read out the refocusing magnetization curve point-by-point. This readout is done by first applying a  $\pi/2$ -pulse to

bring the partially refocused magnetization into the  $z$  axis, and then carrying out the cyclic adiabatic inversion sequence. Then the initial dephasing time  $\tau$  is varied and the readout sequence is repeated. After a set of spin echoes is obtained, the spin-spin relaxation time  $T_2$  can be extracted just as in the conventional NMR discussed in 2.3.2.

#### 2.4.5 Spin Nutation and Calibration of $B_1$

A on-resonance pulse of duration  $t$  tips the magnetization by an angle  $\theta = \gamma B_1 t$  as shown in equation (2.18). Hence by using a RF sequence shown in Figure 2.14, we can experimentally determine the strength of  $B_1$  from the RF coil at the sample location. First, a pulse of duration  $\tau$  is applied to tip the

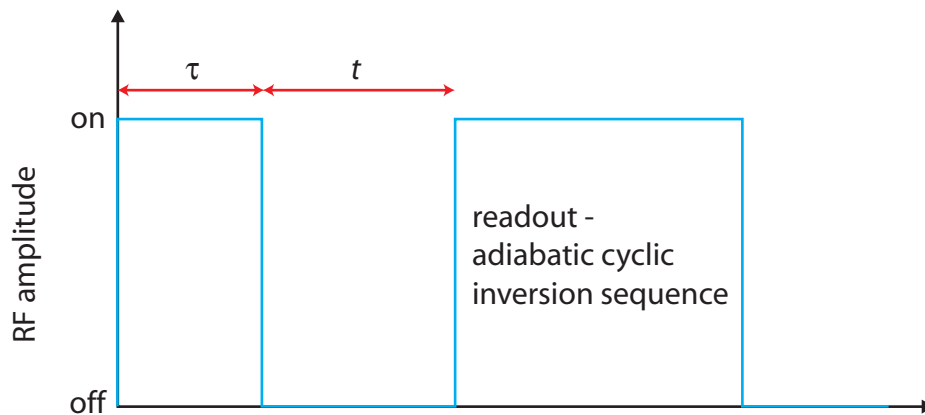


Figure 2.14: RF pulse sequence used for spin nutation experiment.

magnetization by an angle  $\theta$ . Then RF is turned off for some time  $t$  to allow



the  $x'$ - $y'$  plane magnetization to dephase. Then the remaining  $z$  component of the magnetization is readout by the cyclic adiabatic inversion sequence. This procedure is repeated for different  $\tau$ . The resulting data can be fitted to a decaying sinusoid. When the magnetization is tipped  $90^\circ$ , the  $z$ -component of the magnetization will be zero unless there exists an offset in the collected data. This point can be extracted from the fitting and then the strength of  $B_1$  can be obtained. An offset indicates other phenomena at work, such as inhomogeneity, a resonant slice thinner than the sample, spin diffusion from other parts of the sample, etc.; these can be interesting in their own right, but sometimes prevent the accurate determination of  $B_1$  during a nutation experiment.

## Chapter 3

### MRFM Instruments

#### 3.1 Cantilever

Probably the single most crucial part of an MRFM setup is the mechanical cantilever or oscillator. The sensitivity of the apparatus critically depends on the quality and type of mechanical oscillators used because the minimum detectable force is limited by the thermo-mechanical vibration of the oscillators. As mentioned previously, the minimum detectable force is given by the following equation [45]:

$$F_{\min} = \sqrt{\frac{4kk_B T \Delta\nu}{Q\omega_{\text{osc}}}} \quad (3.1)$$

Much progress have been made in fabricating very sensitive cantilevers. In order to improve the sensitivity of the instruments, the cantilever must be free of crystalline defects for high quality factor and must be very soft. As a comparison, a typical tapping mode atomic force microscopy (AFM) cantilever has the spring constant of 1 to 10 N/m, while many of the MRFM experiments use cantilevers with spring constants smaller than  $10^{-2}$  N/m. The quality factor of a mechanical oscillator can be effectively increased by minimizing defects during the course of fabrication and by clever design of the oscillators themselves. Next, I will describe my group's efforts in fabricating double

torsional oscillators for better sensitivity.

### 3.1.1 Introduction to double torsional oscillators

A double torsional oscillator was first used to measure the shear modulus of a thin film [22]. The double torsional design has one apparent advantage over a simple cantilever design. Figure 3.1 shows the first four resonant modes

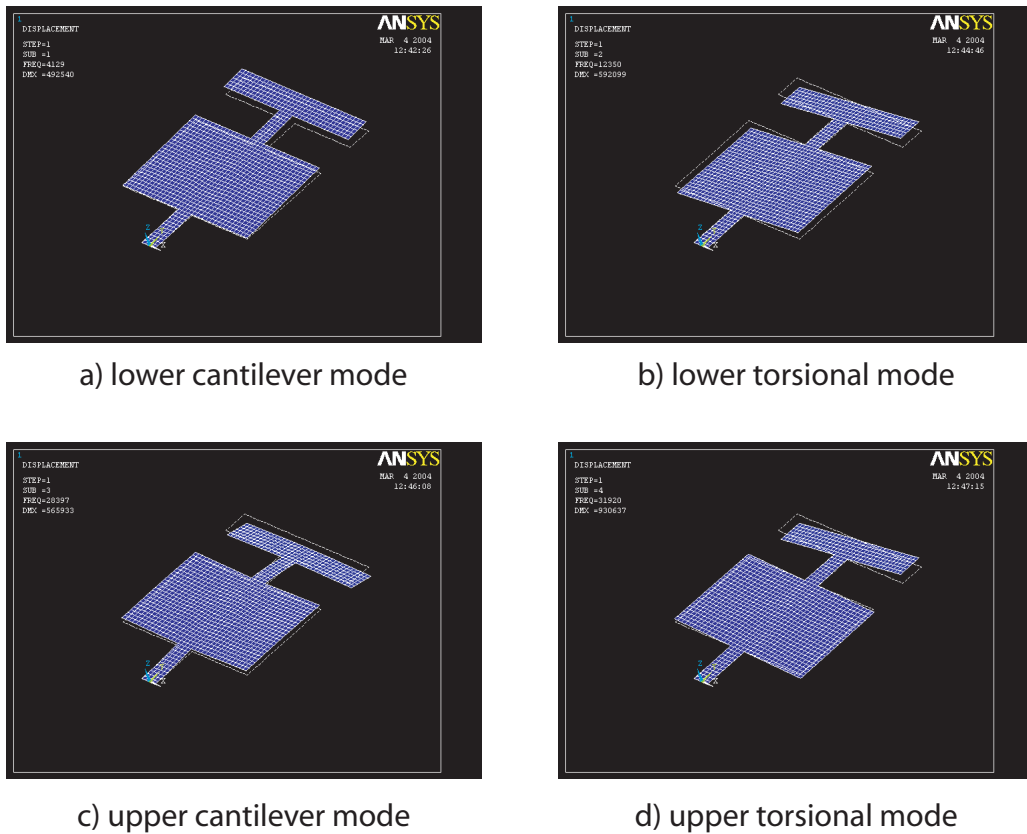


Figure 3.1: First four lowest normal modes of double torsional oscillators. For a description of each mode, see text.

typically measured for double torsional oscillators. The order in which they

appear varies depending on the detailed geometry. However, extensive finite element modeling suggests that those four are usually the first four resonant modes. The lower cantilever mode is characterized by both head and wings swinging back and forth together in phase. This is the usually the lowest oscillator vibrational mode. In the lower torsional mode, head and wings twist about the oscillator's central axis in phase. In the upper cantilever mode, head and wings swing back and forth out of phase. This is illustrated as (c) in Figure 3.1. The upper torsional mode is characterized by head and wings twisting out of phase about the central axis. When a simple angular momentum conservation argument is invoked, one finds that the motion of the smaller head is bigger than that of the wings. This translates into smaller energy dissipation through the narrow neck connecting the oscillator with the rest of the single crystal substrate because of a smaller amplitude of motion near the path of the energy dissipation. This is why, in theory, the upper torsional mode will have a large quality factor,  $Q$ .

### 3.1.2 Fabrication

Figure 3.2 illustrate the process flow for the fabrication of double torsional oscillators. As shown, the entire process involves mostly standard MEMS techniques. The cleanroom in Pickle Research Campus is equipped with most of the process tools needed for a successful fabrication. However, the bulk silicon etching by KOH (potassium hydroxide) is incompatible with CMOS process, and thus performed in our lab.

A blank silicon wafer is implanted with  $^{11}\text{B}$  (boron) across the entire

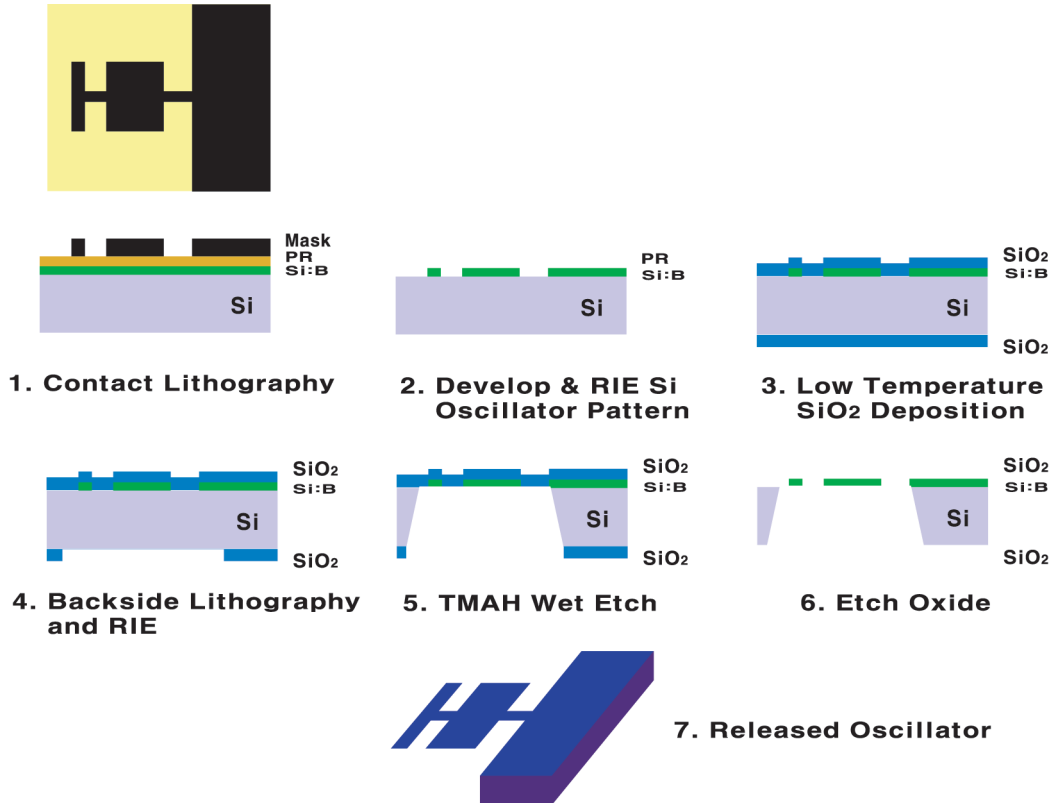


Figure 3.2: Double torsional oscillator fabrication process

one side.<sup>1</sup> Details of the relevant implant parameters can be found [6]. The implanted wafer is ready for optical lithography to define the oscillator pattern on the implanted side. The exposed and developed wafer is then RIE (reactive ion etch) processed to obtain boron-doped silicon oscillator geometry. In order to protect the patterned side from further processing, a 300 nm low temperature oxide is deposited. The available LPCVD (low pressure chemical vapor

<sup>1</sup>Core Systems, Inc. 100 keV implantation energy with  $2 \times 10^{16}$  ions/cm<sup>2</sup> dose.

deposition) furnace deposits low temperature oxide on both sides. The next step requires a back-to-front aligner to precisely align the backside mask to the front side oscillator pattern. I have utilized our own, in-lab, photolithography aligner for this purpose. However, the wafers must be taken outside the cleanroom environment during the exposure. Recently, a front-to-back aligner became available for use in the University's cleanroom. This should be utilized in the future to reduce dust particle related damages that occur during the backside alignment. Once the backside pattern is transferred from the back mask to the wafer substrate, RIE creates openings for the TMAH (tetramethyl ammonium hydroxide) wet etch. TMAH is an all organic silicon etchant that is free of metal ions detrimental to normal CMOS device functions. Hence, it is CMOS process compatible. However, the University's cleanroom does not keep stock of this etchant. Therefore, I carry out wet TMAH silicon etch in our own lab. KOH have been used but because of TMAH's very slow etch rate for  $\text{SiO}_2$ , TMAH was more frequently used for most bulk silicon etching. After the bulk silicon etch is finished, dipping in HF for a short duration removes the protective low temperature oxide. At this point, free standing oscillators can be seen in liquid. The fabricated oscillators are generally thinner than 500 nm. This thinness makes the oscillators very fragile, and the surface tension of drying liquid is sufficiently large to destroy them. Hence, a critical point dryer is used to release oscillators. Figure 3.3 explains the principle behind the critical point drying process. There are several liquids commonly used in critical point drying. The requirement for the liquids is very simple. Their

critical points must be easily accessible. The critical point is the point in the phase diagram above which the phase boundary between liquid and gas disappears. Therefore, there is no surface tension above the critical point. Typically, CO<sub>2</sub> is used for critical point drying fluid for its wide availability, non-toxicity, and easily accessible critical point. The critical point for CO<sub>2</sub> is characterized by the temperature of +31.1 °C and the pressure of 1072 psi. First the sample, in our case cantilever chips, are still in water. The liquid content is slowly replaced with an intermediate fluid. The intermediate fluid of choice is acetone because of its miscibility with both water and liquid CO<sub>2</sub>. Hence, water is first replaced with acetone very slowly as not to break any fragile oscillators. When this process is repeated several times to completely replace water with acetone, the wafers containing oscillator chips are ready to put in the critical point drying chamber. Once the micro-machined structure in a drying boat filled with acetone is put in the drying chamber, liquid CO<sub>2</sub> must be introduced to the chamber very slowly from the liquid CO<sub>2</sub> cylinder. Then the mixed liquid can be drained by opening the drain valve. This must be carried out slowly otherwise liquid CO<sub>2</sub> will evaporate violently and the micro-machined oscillators will break. This process of replacing acetone with liquid CO<sub>2</sub> should be repeated several times to ensure 100 % replacement.

The drying process starts first by raising temperature from point A. As the temperature rises the pressure inside the chamber also rises. As the temperature rises past the critical temperature of CO<sub>2</sub>, the liquid-gas interface disappears and CO<sub>2</sub> enters the phase where there is no distinction between

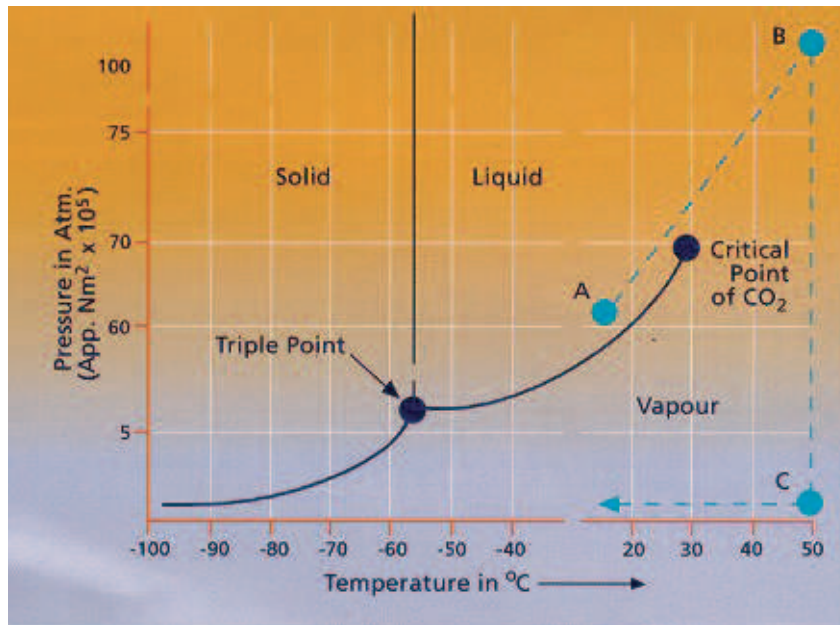


Figure 3.3: Critical point drying using  $\text{CO}_2$ . Point A: Micro-fabricated oscillators are in liquid  $\text{CO}_2$ . Point B: The pressure vessel is closed and the temperature of the vessel is raised above the critical temperature of  $\text{CO}_2$ , which is  $31.1\text{ }^\circ\text{C}$ . Since the pressure vessel is closed, the pressure rises with temperature. Once the temperature is above the critical temperature, the pressure will also be above the critical pressure. Point C: The pressure is released slowly to the atmosphere. The liquid-gas phase boundary has not been crossed, and micro-oscillators are successfully dried without experiencing the surface tension of the gas-liquid interface.

liquid and gas, represented as point B. After getting over the critical point, the pressure inside the chamber is slowly lowered so as not to disturb the supercritical state. If one vents the chamber quickly,  $\text{CO}_2$  will condense into liquid and during this process turbulence will be created. This is detrimental to the successful release of free standing oscillators. Once the bleeding of supercritical  $\text{CO}_2$  is done, one has successfully reached point C without crossing



the phase separating line that divides liquid and gas. Finally, the temperature is lowered, the chamber cover is removed, and free standing oscillators can be removed from the chamber.

### 3.1.3 Characterization

After a successful release of free standing oscillators, their characteristics are measured. Typically, three quantities are measured: resonant frequencies, quality factor, and spring constant.

First, a fabricated oscillator is piezo-electrically driven while lock-in techniques are used to measure its frequency behavior. Figure 3.4 describes the general experimental configuration. Red lines in the figure represent optical signals, while blue lines represent electrical signals. Optical components will be described in further detail in the next section. The manual for Stanford Research System's SR830 lock-in amplifier has an excellent discussion of the lock-in technique, from what it is to how it should be used in an experiment. All relevant parameters for proper use of a lock-in amplifier are very important, and their meanings should be carefully understood before any measurement is taken. Figure 3.5 shows one example of a frequency scan. The voltage signal can be later converted to displacement. When fitted with a Lorentzian, two important parameters can be extracted, the resonant frequency,  $\omega_c$ , and the quality factor,  $Q$ .

The spring constant of an oscillator also needs to be measured in order to calculate the sensitivity of the oscillator. There have been several different

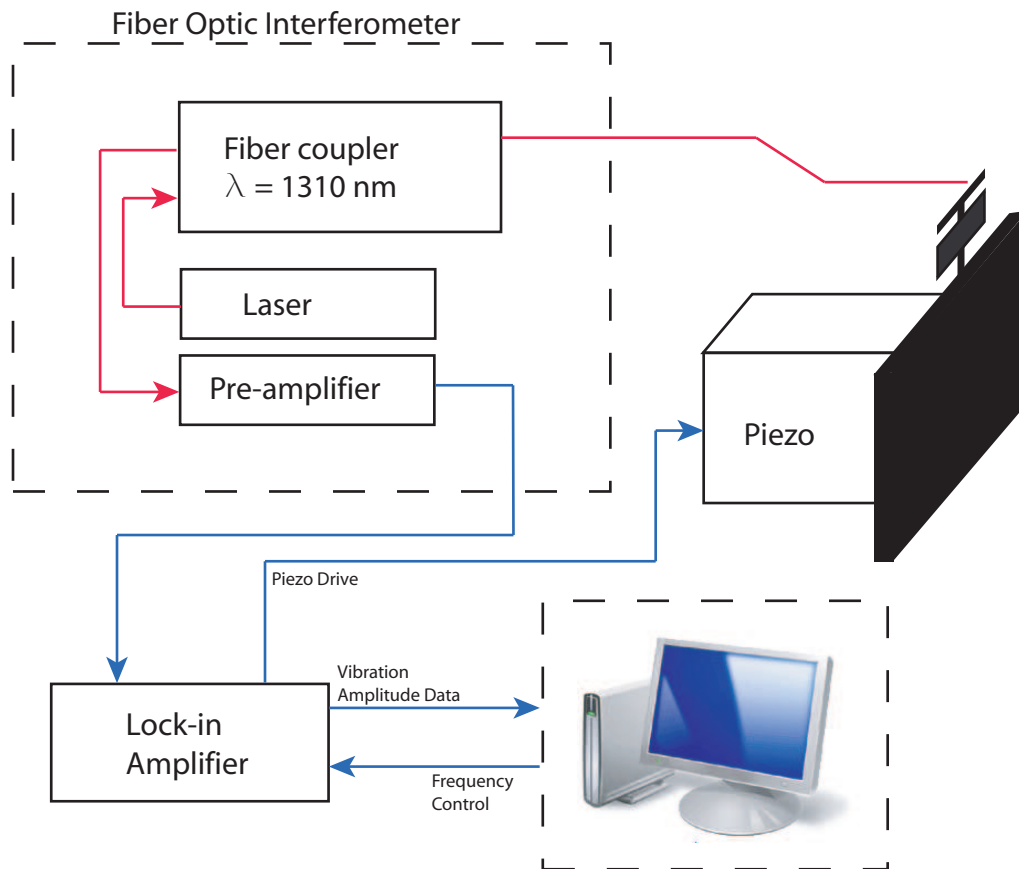


Figure 3.4: Configuration for driven scans for measuring resonant frequencies of oscillators. Red lines indicate optical signal paths, while blue lines indicate electrical signal paths.

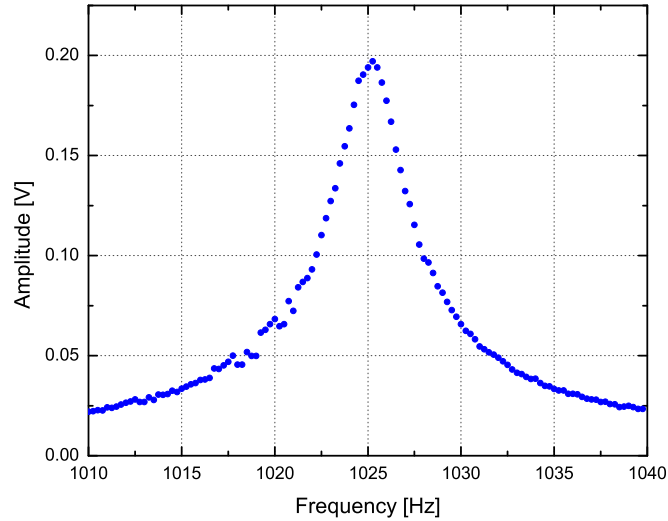


Figure 3.5: An example of resonant frequency scan. Scans can be fitted to Lorentzian to extract the precise location of the peak and the quality factor of resonance

methods in determining the spring constant including a direct calculation from the known geometry [5, 10, 42], an inference from the thermal-noise [20], and others. We have used the approach in [20] to determine the spring constants of oscillators used. The method relies on the fact that in thermal equilibrium the harmonic oscillator's energy is equal to the thermal energy. This is to say

$$\frac{1}{2} k \langle x^2 \rangle = \frac{1}{2} k_B T \quad (3.2)$$

Thus, when one knows the equilibrium temperature and the amplitude of thermal vibration, the spring constant  $k$  can be determined. The amplitude of thermal motion is determined from the power spectral density estimate using

the Welch method [35]. The power spectral density (PSD) describes how the power of a signal or time series is distributed with frequency. Since the square of the amplitude is proportional to the power, the PSD can be used to extract the amplitude of thermal motion. In general terms, one way of estimating the PSD of a process is to calculate the discrete-time Fourier transform (DFT) of the time series of the motion and take the magnitude squared of the result. This is called the periodogram. It is an estimate since only a finite-time sample is used for calculation.<sup>2</sup>

The measurement process is described next. If the resonant frequency of an oscillator under investigation is, say, 3 kHz, even a moderately fast digitizer will be able to record a time-series data needed for DFT.<sup>3</sup> However, we decided to use a lock-in amplifier because we want to reject all other frequency components except those around the resonant frequency. The lock-in amplifier's reference frequency is set slightly off the resonant frequency<sup>4</sup> and the discrete time samples are recorded into the lock-in amplifier's internal buffer. One must choose the time constant and the sampling rate properly. The time constant must be set to include the entire resonance curve. Once the bandwidth of detection is determined the sampling rate can be chosen to be at least twice the bandwidth. Then the DFT is performed on the time-series data, and

---

<sup>2</sup>for a thorough mathematical treatment refer to [50].

<sup>3</sup>Nyquist theorem states that the discrete samples are a complete representation of the signal if the bandwidth is less than half the sampling rate.

<sup>4</sup>This is to avoid a large DC error that may swamp the signal of interest. Since a lock-in amplifier acts as a mixer if one sets the reference frequency to the signal frequency, the output will be DC.

the result is squared to obtain the PSD. One must use the complex DFT instead of real DFT. This is needed because the lock-in amplifier acts as a low pass filter centered at the reference frequency with the bandwidth determined by the time constant. In order to distinguish whether a signal is from below or above the reference frequency, the phase information must be kept throughout the complex DFT. The PSD can be fitted to a Lorentzian, and the integration is performed to calculate the amplitude of motion. Figure 3.6 contains an example of the PSD graph. As they should, the resonant frequency and the quality factor measured from the three different methods agree very well. One note about the ring-down measurement is needed. Since the lock-in amplifier is used as a mixer, the difference in the frequency between the reference and the cantilever resonant frequencies is shown in the graph. One must know beforehand whether the reference frequency for the lock-in amplifier is either lower or higher in order to calculate the cantilever resonant frequency.

### **3.1.4 Fiber Optic Interferometer**

Most of MRFM probes in various research groups have fiber optic interferometers for detecting angstrom-scale motion [14, 16, 38, 41, 52]. There have been cases where a beam-bounce technique[23], typically employed by ambient condition atomic force microscopes, or a piezoresistive cantilever technique[48] is used for measuring vibrational amplitudes. The beam-bounce technique is not suitable for cryogenic temperatures since the laser and the photodiode cannot be located far from the mechanical oscillator. Piezoresistive cantilevers

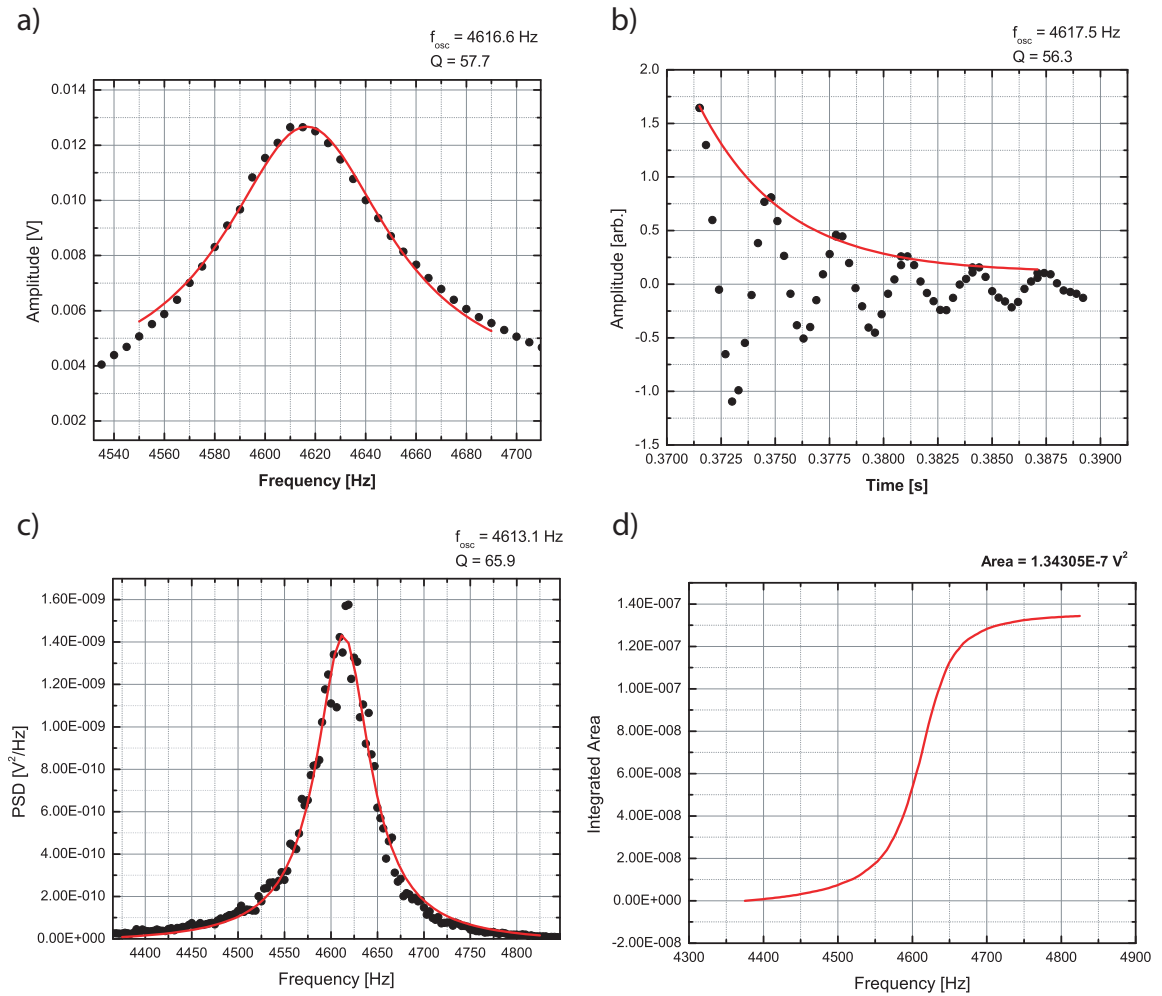


Figure 3.6: Typical measurement results. a) Driven scan. b) Ring-down measurement used to determine the quality factor. c) PSD estimation by the modified Welch method. d) Integrated area under the curve in c). Red curves are fits to the data.

have an advantage in that they do not need any optical components. However, their sensitivity is not as good as fiber optic interferometers.

As shown in Figure 3.7, our interferometer operates at 1310 nm. The 2x2 coupler installed in the low temperature probe is a DWC (Dual window coupler). It has two operating bandwidths;  $1310 \pm 40$  nm and  $1550 \pm 40$  nm. The power from the laser can be varied by controlling the laser current.

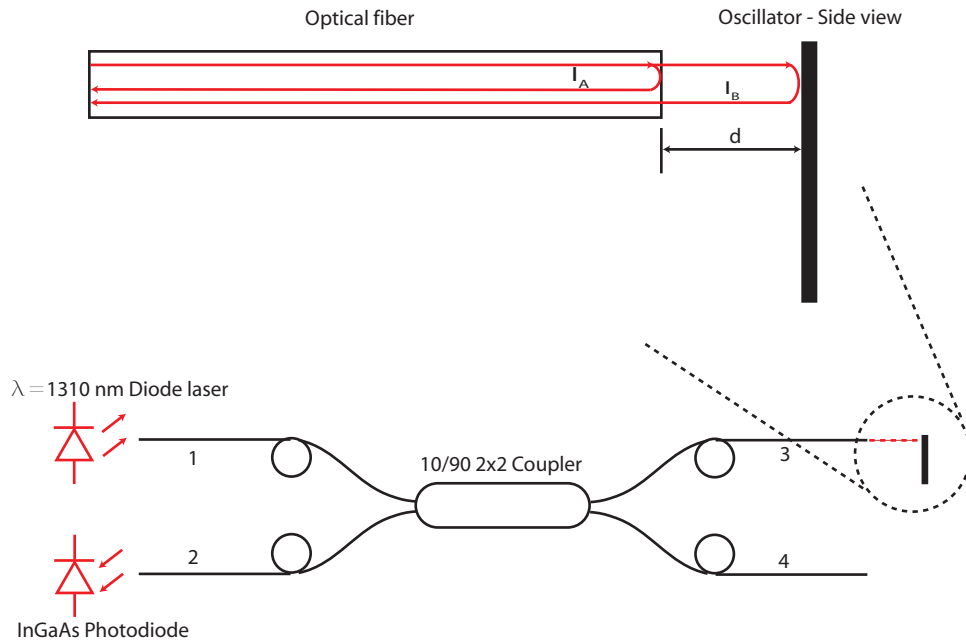


Figure 3.7: Fiber optic interferometer used in current setup. The photodiode is also sensitive for a 1550 nm laser. A 1550 nm laser will reduce heating of oscillators, but the overall sensitivity of displacement measurement decreases.

Because the photon energy for a 1310 nm laser is smaller than the silicon bandgap, laser heating of an oscillator is not significant. However, we usually drive the laser well below 1 mW to reduce heating of the surrounding area. For example, the diode laser currently used in the experiment is rated 1 mW with

24.8 mA of current. However, we feed only 20 mA. We still have a big enough signal to work with as long as the alignment is good. Because the laser power is not a linear function of current due to its intrinsic nonlinear behavior, we do not have a known power output from the laser when a reduced current is used.

The first optical fiber interferometer for a force microscope is discussed in detail in [37]. As shown in Fig. 3.7, two laser beams labelled  $I_A$  and  $I_B$  interfere and produce an interferometric signal as a function of the distance,  $d$ , between the cleaved fiber end and the oscillator. The system achieves a constructive interference when

$$2d = \left( n + \frac{1}{2} \right) \lambda \quad (3.3)$$

Similarly, the condition for a destructive interference is given by

$$2d = n\lambda \quad (3.4)$$

In order to maximize the sensitivity, the interferometer must operate at the point where the slope of the fringe is the maximum. This is to say the cavity separation  $d$  is chosen so that DC signal from the interferometer is at the maximum slope of the fringe. Figure 3.8 illustrates this graphically. The photodiode signal as a function of displacement from the fringe center is given by

$$V_{\text{sig}} = V_{\text{off}} + A \sin \left( \frac{2\pi}{\lambda/2} x \right) \quad (3.5)$$

$V_{\text{off}}$  is a term due to the fact that two interfering branches  $I_A$  and  $I_B$  are not equal.  $I_A$  is approximately 4% of incident laser power for an optimally cleaved



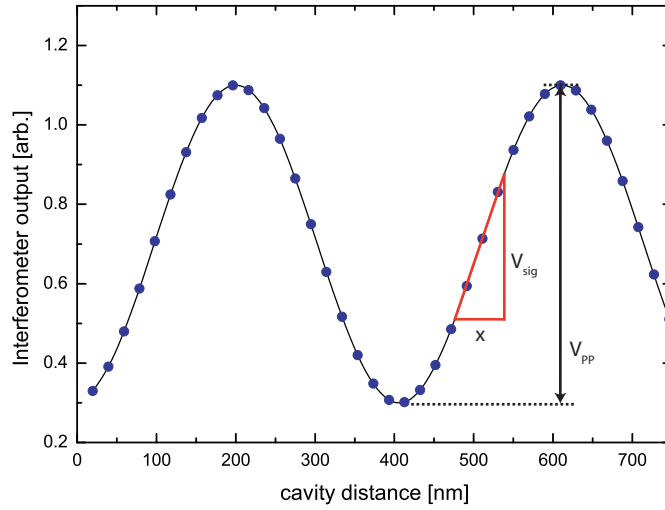


Figure 3.8: A typical interference fringe as a function of interferometer cavity length. The interferometer should be operated at the center of the fringe in order to use the linear approximation for small changes in signal.

end.  $I_B$ , however, can vary greatly depending on the alignment between the cleaved end of the optical fiber and the oscillator, reflectivity of the oscillator surface, the cavity length, and others. For a small amplitude vibration near the fringe center, a conversion factor from the voltage reading to displacement can be obtained by taking a derivative of the equation (3.4) and evaluating at  $x = 0$ .

$$\begin{aligned}
 \left[ \frac{dV_{\text{sig}}}{dx} \right]_{x=0} &= \left[ A \frac{2\pi}{\lambda/2} \cos \left( \frac{2\pi}{\lambda/2} x \right) \right]_{x=0} \\
 &= \left[ 2A \frac{2\pi}{\lambda} \cos \left( \frac{2\pi}{\lambda/2} x \right) \right]_{x=0} \\
 &= \frac{2\pi}{\lambda} V_{\text{PP}}
 \end{aligned} \tag{3.6}$$

$V_{\text{PP}}$  is the peak-to-peak value of the interference fringe as shown in Figure 3.8. Therefore, one can now obtain the actual displacement value in meters from

the photodiode voltage output. One must be careful, however, in that the lock-in amplifier normalizes its outputs to 10 V full scale. The corresponding gain is a function of the lock-in sensitivity. Hence, if one uses normalized outputs for calculations, the actual values measured by a lock-in amplifier will be given by

$$V_{\text{actual}} = V_{\text{lock-in}} \frac{\text{sensitivity}}{10} \quad (3.7)$$

In principle, one can further minimize the laser heating by using a 1550 nm laser. Also, a better stability of the laser wavelength can be achieved by the use of a DFB (distributed feedback) laser diode. If one ultimately wants a single photon sensitivity, an avalanche photodiode must be incorporated into the design.

## 3.2 RF components

Because MRFM is similar to NMR, many aspects of an experimental setup overlap. RF (radio-frequency) components are one of them. One difference between solid-state NMR and MRFM experiments is the power level used. In a solid-state NMR experiments, often powers exceeding 100 W are used. However, in a typical MRFM experiment, only up to a few watts of power are needed due to the smaller RF coil volume. A coil is used to generate an electromagnetic wave typically in the radio-frequency region of the spectrum to induce resonant level transitions in a sample. At such frequencies, an ordinary coaxial cable has a non-negligible capacitance and inductance, and thus has the corresponding capacitive and inductive reactances. When there is

an impedance mismatch at a cable interface, most of the power gets reflected. Hence, in order to most efficiently transfer power from the amplifier to the RF coil, the tank circuit's (collective term for NMR coil, tuning and matching capacitors) impedance must be matched to that of the amplifier output (typically  $50 \Omega$ ).

Figure 3.9 shows a schematic of RF tank circuit. With the help of a

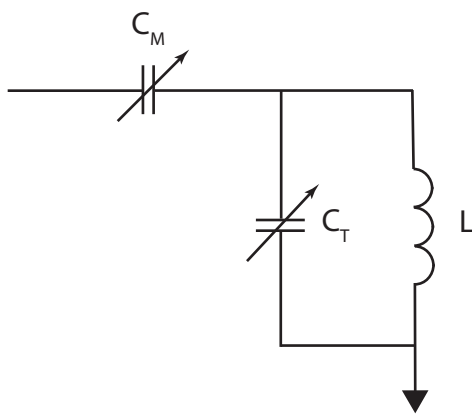


Figure 3.9: RF tank circuit: series matched and parallel tuned circuit.

network analyzer, a 1-port reflectance measurement can be used to adjust the tank circuit's impedance to  $50 \Omega$ . First, the network analyzer's center frequency and span are set to desired values. Then, the three-point calibration is run: open, close, and load ( $50 \Omega$ ). After the calibration, the network analyzer computes necessary coefficients required for correct readings at the previously set frequency. Once the calibration is done, the impedance of the tank circuit can be matched to  $50 \Omega$  by adjusting the matching,  $C_M$ , and tuning,  $C_T$ , capacitors.

It is often desirable to know  $B_1$  in the coil for the given amount of

power. However, it is nontrivial to estimate the power from a small coil with the diameter less than 1 mm. Also, the fact that a sample does not reside in the coil but some finite distance away from the plane of the coil makes the field strength estimation difficult. For a solid state  $^1\text{H}$  NMR experiment, a  $B_1$  field of on the order of 5 G or more is needed in order to overcome local fields due to nuclear spin-spin interactions and to manipulate spins. For a macroscopic coil,  $B_1$  is given by

$$B_1 = \left[ \frac{\mu_0 P Q}{2\omega V_c} \right]^{1/2} \quad (3.8)$$

where  $P$  is the power delivered to the coil,  $\omega$  is the frequency,  $Q$  is the loaded quality factor of the NMR tank circuit, and  $V_c$  is the volume of the coil. In order to utilize this formula, one must know the loaded quality factor of the NMR tank circuit. Other research groups have used a value on the order of 100 for  $Q$  [15, 41]. High  $Q$  allows bigger  $B_1$  with small power, but because of its narrow frequency band tuning must be maintained precisely. In addition, in an MRFM experiment, the carrier frequency is frequency-modulated, so a very narrow frequency band, i.e, high  $Q$ , is not so desirable, i.e., it puts a limit on the modulation depth. The strength of  $B_1$  can be experimentally determined from the nutation measurements as discussed in 2.4.5.

In the current  $^3\text{He}$  low temperature probe, variable capacitors for the tank circuit cannot be placed close to the coil due to a space constraint. So we have adopted a remote tuning method [47]. In this geometry, series and parallel capacitors are placed close to the NMR coil to roughly tune to the desired operating frequency. This fixed frequency tank circuit is connected to a set

of variable tuning and matching capacitors located conveniently outside the probe. These variable capacitors are used to tune exactly to the operating frequency. Both theoretical and experimental studies of such geometry revealed that the tank circuit's efficiency can be improved significantly. However, the efficiency, at best, is comparable to that of a locally tuned tank circuit.

### **3.3 3-Axis Piezoelectric Positioners**

The control needed for fine positioning is provided by two independent 3-axis piezoelectric stages. The design concept is borrowed from Attocube Systems' nanopositioners. Figure 3.10 shows 3-dimensional CAD-constructed view of the assembled stage. Figure 3.10 shows only one set out of two 3-axis stages. In the actual setup, two stages are employed: one for positioning the fiber optic interferometer with respect to a cantilever and one for positioning a magnetic field gradient-producing magnet or a sample with respect to the cantilever depending on the experimental configuration. Figure 3.11 shows how the positioners are incorporated into the design.

The inertial positioners are made of titanium because of its light weight and non-magnetic properties. Titanium has been used in other low temperature, high magnetic field applications [12, 19]. In principle, OFHC (oxygen-free, high conductivity) copper can be used. However, this will require a more careful design that can reduce the weight of each piece used in the positioners. Also, because the coefficient of friction of the copper surface is not small enough to allow a smooth sliding motion with a small applied force, a different

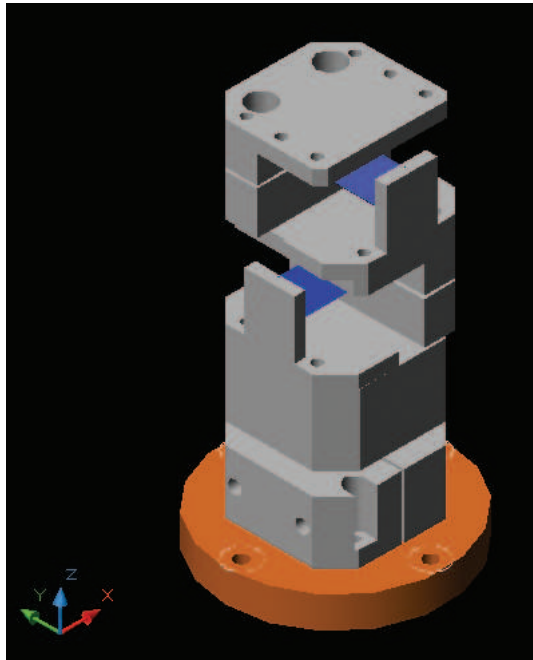


Figure 3.10: 3-dimensional CAD view of 3-axis positioner.

sliding surface should be used, say sapphire or polished alumina. This possibility had been explored in the prototyping stage and had been proven to work. However, in the final design a polished titanium surface was preferred.

The controller that drives piezo stacks has been designed to address all six axes with dedicated drivers. Hence, each axis has its own driver and, in principle, can be calibrated for the step size with its dedicated amplifier channel. This allows us to fix either the driving voltage or frequency for each channel and to settle on some semi-permanent values. The controller is designed around Microchip's 8-bit PIC<sup>TM</sup> micro-controllers for their wide availability and ease of programming. PIC<sup>TM</sup> microcontrollers with flash memories can be easily programmed with various versions of programmers available on

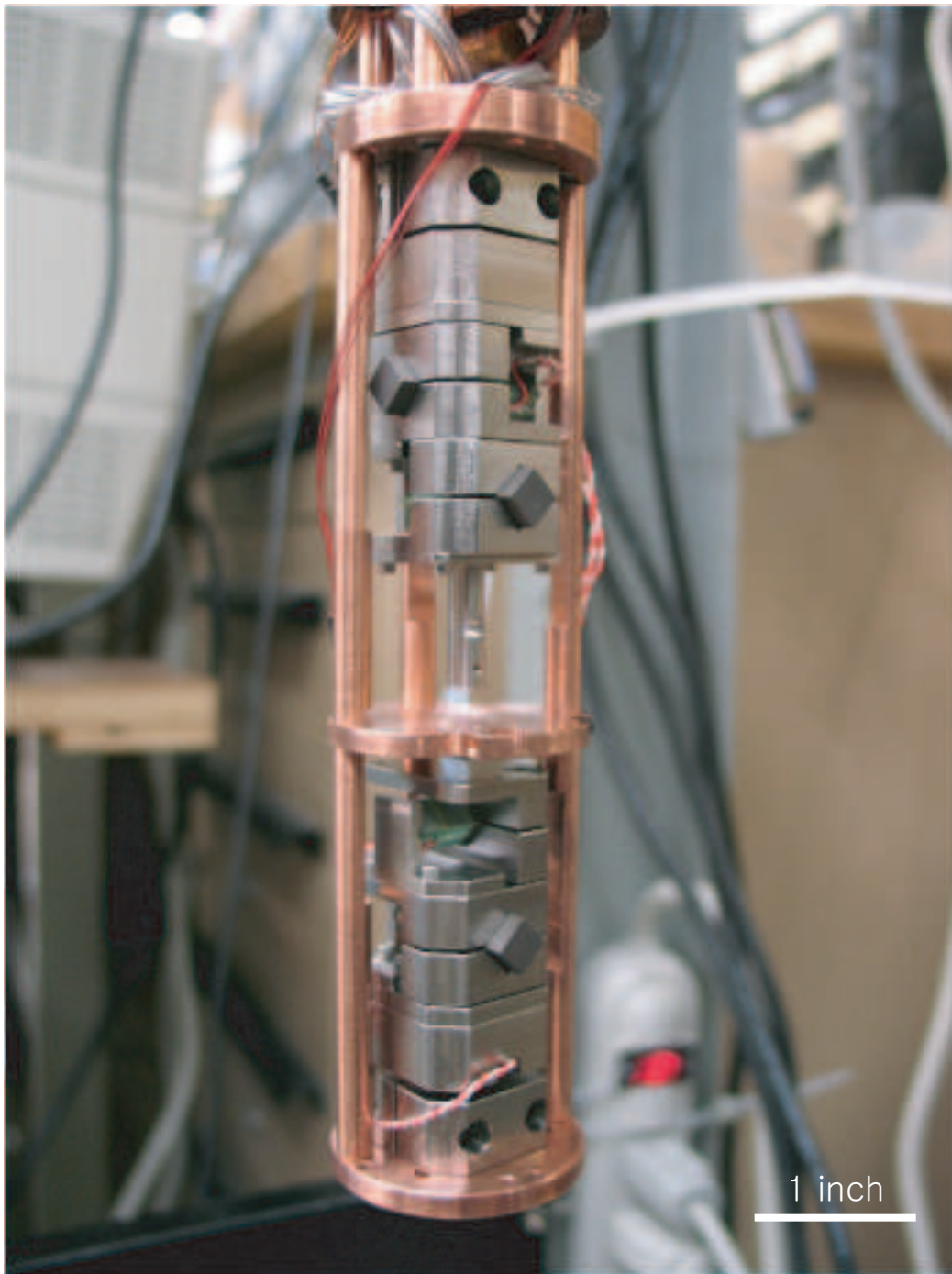


Figure 3.11: Picture of both stages installed in the probe. The RF board containing RF circuitry and cantilever mount are not shown.

the internet. PIC™ assembly is also easy to learn due to a small number of commands to master. Figure 3.12 shows the functional block diagram of the controller. It can be decomposed into two parts. The first part is responsible for generating a sawtooth waveform either continuously or one waveform at a time. The second part of the controller is responsible for amplifying the 5 V waveform to a user configurable level. Red arrows indicate analog signal paths, while blue arrows indicate digital signal paths. More complete schematics of

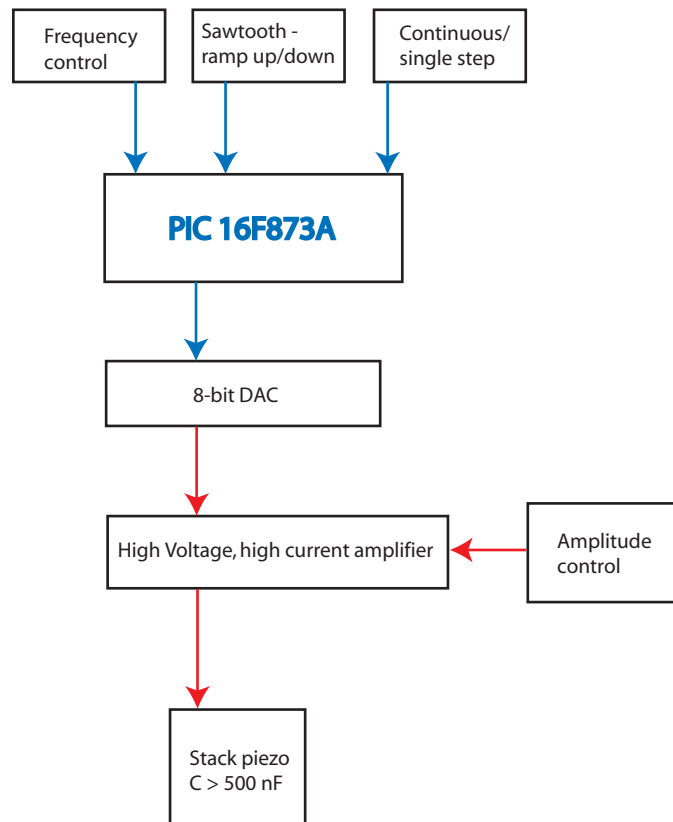


Figure 3.12: Block diagram for the inertial positioner controller. Blue lines indicate digital signal paths, while red lines indicate analog signal paths.



the controller can be found in Appendix B.

# Chapter 4

## Experiments

### 4.1 Magnetic Field Gradient

MRFM exploits the coupling between the sample magnetization and the magnetic field gradient  $\nabla B$  produced by a ferromagnetic particle or a permanent magnet. The thickness of the so-called resonant slice in which the sample is under magnetic resonance is given by

$$\Delta z = \frac{2\Omega/\gamma}{\nabla B} \quad (4.1)$$

where  $\gamma$  is the gyromagnetic ratio and  $\Omega$  is the FM depth as discussed in Chapter 2. In order to obtain a better resolution, i.e., smaller resonant slice thickness, the magnetic field gradient must be large. This is one area of active MRFM research where others tried to image samples with a large gradient magnet [3]. Since the dipole field of the magnet is usually considered, the magnet-sample distance is shortened in order to achieve bigger gradients. As the magnet-sample distance shrunk, there have been unwanted and unanticipated effects that complicate measurements such as electrostatic forces, or magnetic and electric dissipations, that obscure the MRFM signals. However, in our present experiment, the magnet is situated far ( $\sim 1$  mm away) from the sample and the above mentioned problems can be ignored.

The resonant field is the sum of the external field generated by a superconducting magnet and the field generated by a gradient-producing magnet. At present, an iron cylinder 0.050" in diameter and 0.500" in length is used as the gradient-producing magnet. Iron was chosen for its large saturation magnetization and small coercivity. Small coercivity ensures that iron's magnetic moments are easily aligned to the applied field. Also, even a small applied field will be sufficient for a full saturation. Other groups have used different types of magnets: AlNiCo[16], PrFeB[8], and other rare-earth based hard magnets. Figure 4.1 and 4.2 show the calculated magnetic field and the gradient,

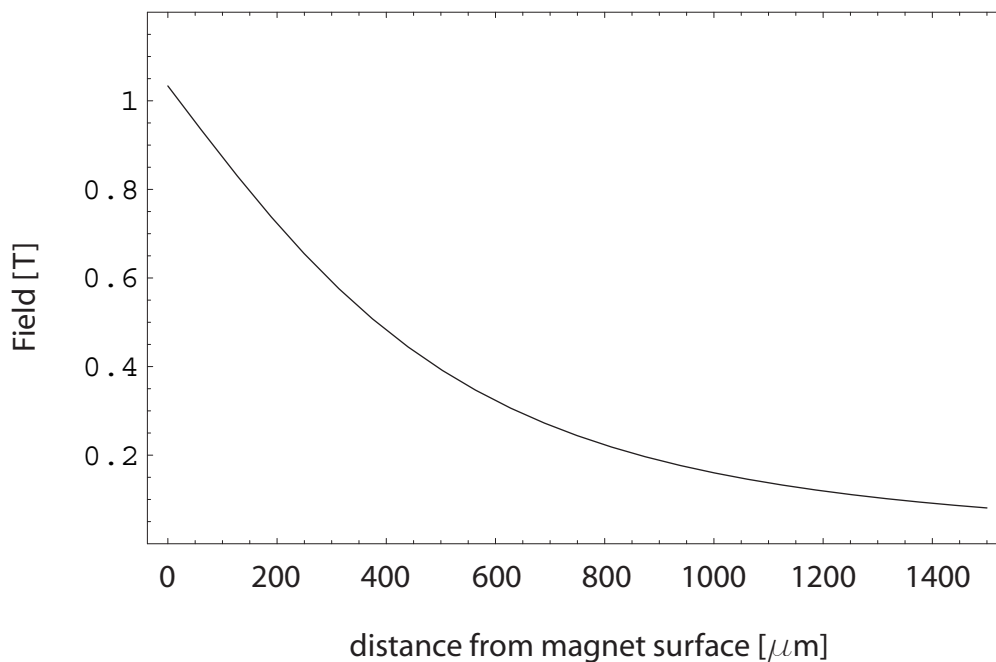


Figure 4.1: Calculation of magnetic field from the fully saturated iron cylinder with dimensions given in the text. This field will need to be added to the field from the superconducting magnet in order to correctly calculate the resonant field.

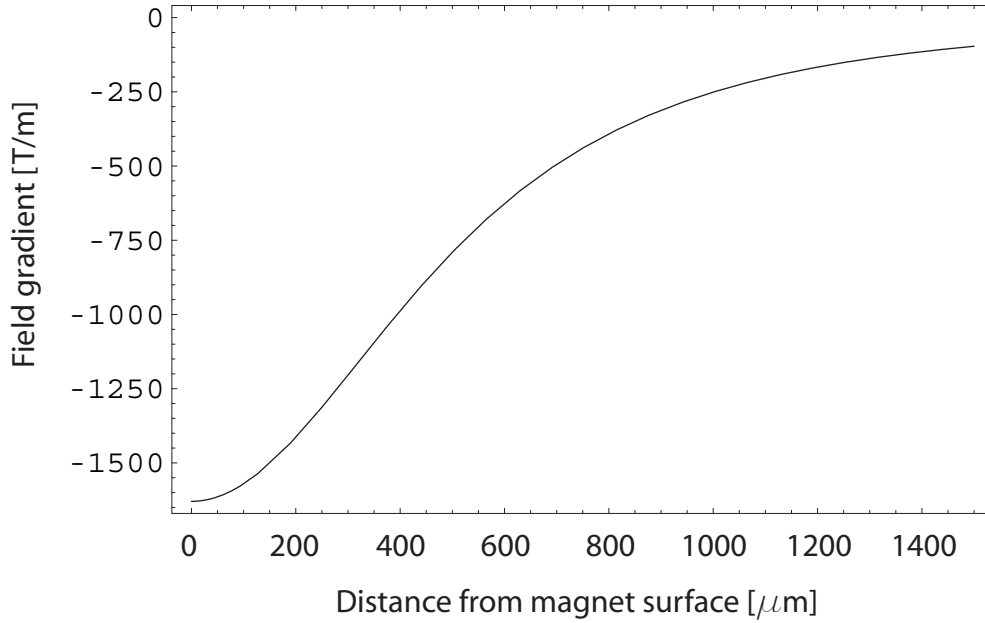


Figure 4.2: Calculation of magnetic field gradient from the fully saturated iron cylinder with dimensions given in the text. Once the operating distance is determined, the resonant slice thickness can be estimated by (4.1).

respectively, from the fully saturated iron cylinder with the previously mentioned dimensions as a function of the distance from the magnet face. In order to utilize a large gradient from the iron cylinder, one must place the magnet close to the sample. However, due to the finite size of the RF coil, there is a limit to how close we can place the iron magnet to the sample. Since the diameter of the typical RF coil used in the present setup is about  $800 \mu\text{m}$ , the iron magnet can get within only  $\sim 500 \mu\text{m}$  from the sample which is mounted at the end of a cantilever.<sup>1</sup>

---

<sup>1</sup>See Figure 2.9 for the relative, schematic placement of various components in the experiment.

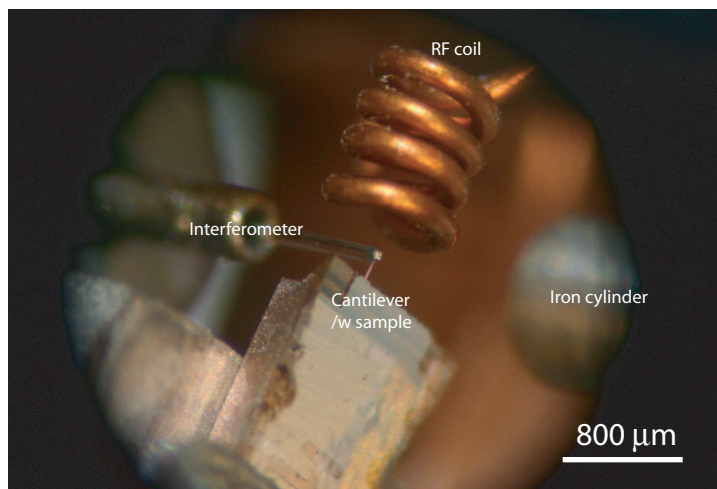


Figure 4.3: Close-up picture showing components and their relative positions. The cantilever shown is  $200\ \mu\text{m}$  long. The iron cylinder is normally placed within 1 mm from the sample. It has been backed up in order to not block the view of other components.

## 4.2 Initial Attempt to Observe Force-detected MRFM

We have chosen  $(\text{NH}_4)_2\text{SO}_4$  as the sample for our initial experiment for two reasons: its well known NMR relaxation time data<sup>2</sup> and a high hydrogen density. Previously, the field from the Cryomagnetics NMR magnet was measured to be 8.07 T.<sup>3</sup> Since we have chosen the separation between the sample and the iron cylinder to be 1 mm, the resonant field became 8.23 T ( $=8.07+0.16$ ). Then the Larmor frequency is 350.433 MHz. Since the sample loaded cantilever's mechanical resonant frequency was measured to be 1.6 kHz, the FM depth was chosen to be 150 kHz without violating the adiabatic

<sup>2</sup> $T_1 \sim 2\ \text{s}$  at room temperature [23]

<sup>3</sup>Utkur Mirsaidov, private conversations

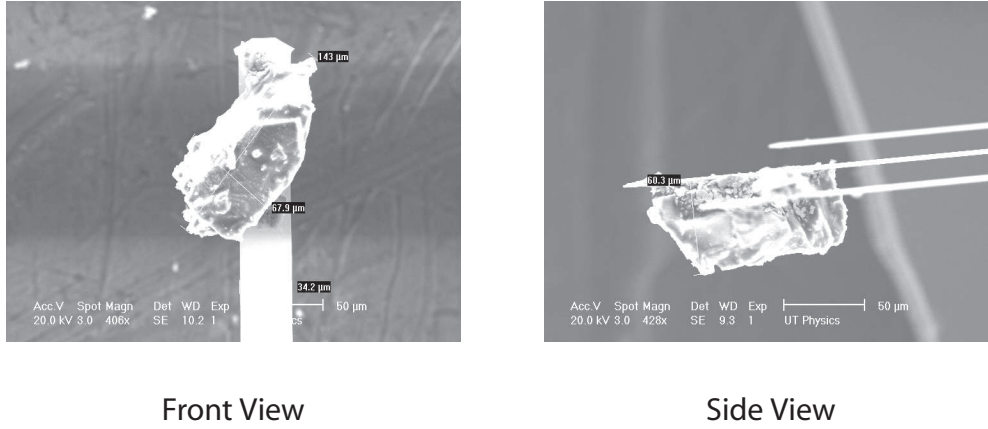


Figure 4.4: SEM image showing a sample attached at the end of a cantilever.

condition. The adiabatic condition for the triangular modulation is calculated as

$$\Omega \ll \frac{\gamma^2 B_1^2}{4f_{\text{osc}}} = \frac{((42.58 \text{ MHz/T}) (15 \text{ G}))^2}{4(1.6 \text{ kHz})} = 637 \text{ kHz} \quad (4.2)$$

where we have assumed that  $B_1 = 15 \text{ G}$ . The resonant slice thickness is calculated to be  $\sim 28 \mu\text{m}$ . We intentionally chose a big number so that the signal would be large. If we successfully observe a force-detected NMR signal, the depth of frequency modulation  $\Omega$  can be decreased to improve the resolution. However, the resonant slice cannot decrease to an arbitrarily small value because of the fundamental thermal noise limit on the force resolution of the cantilever used. In order to obtain a still better resolution, one must utilize a higher gradient. Figure 4.4 shows SEM images of the sample mounted cantilevers.  $(\text{NH}_4)_2\text{SO}_4$  samples are mounted at the end of the cantilever with a dab of silver epoxy. Therefore, the added mass comes not only from the sample but also from the epoxy dab as well. However, the amount of epoxy

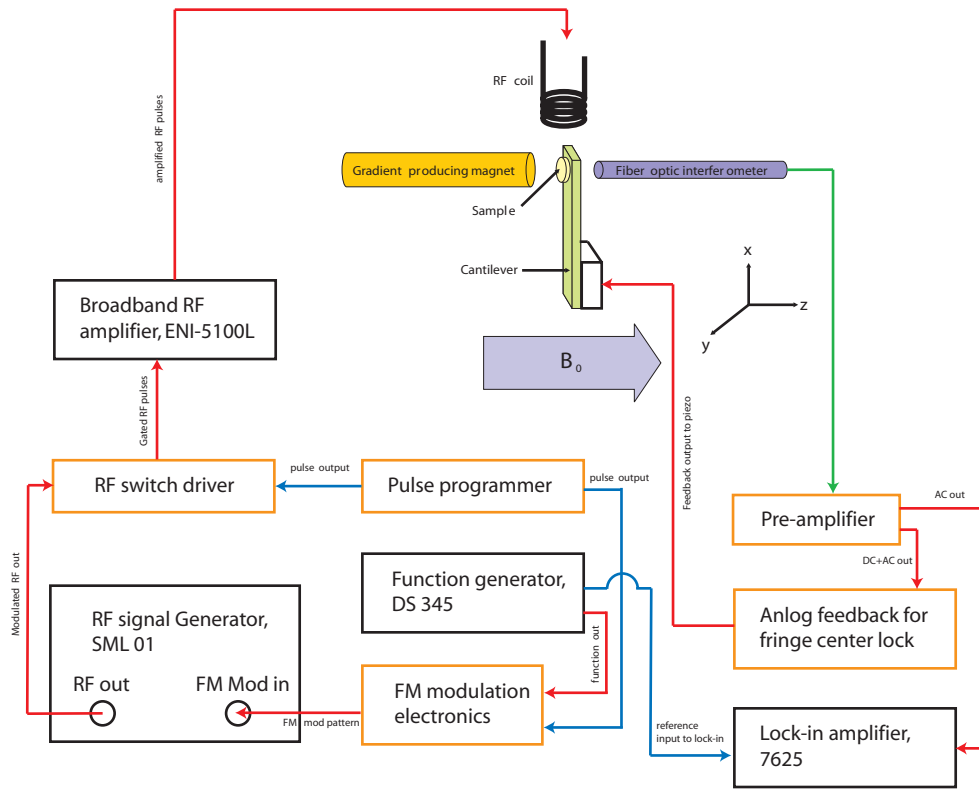


Figure 4.5: Block diagram showing various connections for the experiment. Green lines indicate optical signal paths, red lines indicate analog signal paths, and blue lines indicate digital signal paths. Orange boxed parts indicate home-made components. The positioner and its electronics for advancing and retracting the iron magnet and fiber are not shown in the diagram.

used was minimized, and its mass contribution should be small.

When a cantilever with a mounted sample is prepared, every piece of an experiment is ready for assembly. Figure 4.5 shows how our electronics for an experiment are connected. The FM electronics described in Appendix C is used to generate a FM voltage pattern which is fed to the modulation input of the RF signal generator. The timing of the FM is controlled with

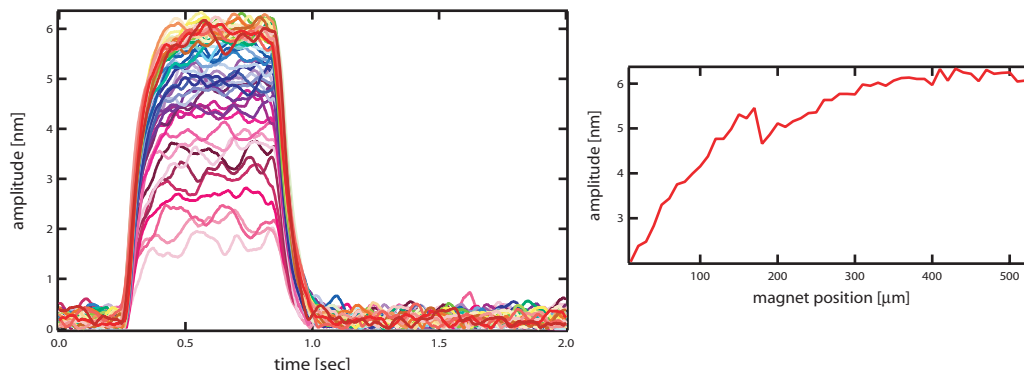


Figure 4.6: Typical single-sweep data and amplitude plot as a function of magnet-sample distance.

a set of homemade pulse programmers [8] and a switch driver. The properly modulated and gated RF is then amplified by a broadband RF amplifier with a gain of 50 dB and sent to the RF coil. The resulting cantilever vibration is detected synchronously with a lock-in amplifier referenced to the same FM frequency.

Our initial attempt at detecting a force-detected  $^1\text{H}$  NMR signal from  $(\text{NH}_4)_2\text{SO}_4$  was not successful. Typical single-sweep data is shown in Figure 4.6. The spurious excitation grows in amplitude as the gradient-producing iron cylinder moves out of the region directly beneath the RF coil. Since the RF coil's diameter is  $800\ \mu\text{m}$ , the spurious excitation grows until the magnet-sample distance is about  $400\ \mu\text{m}$  as shown in Figure 4.6. We then investigated possible causes for the unsuccessful detection.



### 4.3 Troubleshooting

First, we needed to verify the field from our NMR magnet was indeed 8.07 T as measured by previous lab members. The change in field strength of the magnet was a very unlikely scenario. However, it could be easily checked by performing conventional NMR on a suitable liquid sample. Unfortunately, we could not perform  $^1\text{H}$  NMR at 8.07 T because our NMR spectrometer [7] is limited to 160 MHz.<sup>4</sup> However,  $\text{D}_2\text{O}$  is readily available and because of deuterium's small gyromagnetic ratio of 6.536 MHz/T, we decided to look for deuterium resonance at 52.745 MHz ( $= 6.536 \times 8.07$ ). The velocity factor for RG-58 coaxial cable is 0.66 [1]. So the wavelength of 52.745 MHz RF in the RG-58 coaxial cable is  $\sim 3.75$  m. Hence, we tried to keep the cable length between the RF coil and variable capacitors to less than 1.87 m or less if possible. The reason for limiting cable lengths is because a higher quality factor of the tank circuit is better in a convention NMR experiment. In force detected NMR this requirement is not as stringent as in conventional NMR. However, in order to effectively generate  $B_1$  with a small power, a higher quality is often desired.<sup>5</sup> In many instances, placing variable capacitors close to the RF coil is impossible due to space limitations, and a  $\lambda/2$ -cable is used to connect the RF coil and the variable capacitor [13]. Ideally, a  $\lambda/2$ -cable acts as if there is no cable at all, i.e., the RF coil is attached to the variable

---

<sup>4</sup>For a detailed description of the heterodyne NMR spectrometer, refer to [7]. [11] contains information on modifications made to the original design.

<sup>5</sup>Because of the FM RF carrier, the quality factor should not be made too large. Other groups claimed to use tank circuits with quality factors around 100.

capacitors without the cable.

After successfully setting up the spectrometer, we were able to detect a deuterium NMR signal at 52.716 MHz. Knowing  $\gamma = 6.5359$  MHz/T, the resonant field was calculated to be 8.0656 T. This number is within 0.5% of the number we assumed before the experiment.

Second, we were not sure whether we had enough  $B_1$  field strength to manipulate sample spins. For solids samples, the local field seen by each nucleus is on the order of few gauss. Therefore, we needed to make sure that the  $B_1$  field from our RF coil is big enough to overcome the local fields in order to successfully manipulate spins during cyclic adiabatic inversion.

Thus, we extended our NMR experiment to millimeter-size RF coils and were able to observe a deuterium NMR signal from a very small deuterium oxide sample. By measuring the length of either the  $\pi/2$ -pulse or the  $\pi$ -pulse, we should be able to calculate the strength of  $B_1$  field strength from equation (2.18). However, there were two things that still need to be addressed. First, the millimeter-size RF coils used in this conventional NMR experiment were larger than the sub-millimeter-size RF coils used in force-detected NMR experiments. However, given the fact that all other parameters stayed the same except the RF coil dimension, the strength of  $B_1$  should increase with the decrease in volume of the coil. Therefore, we would expect the strength of  $B_1$  to be better for the slightly smaller RF coil used in a force-detected NMR experiment.<sup>6</sup> Second, the field we would obtain from the measurement

---

<sup>6</sup>See (3.7) for the exact relation between RF coil parameters and the strength of  $B_1$ .

of either the  $\pi/2$  or  $\pi$  pulse length would be at the center of the solenoid coil. In a force-detected NMR experiment, a sample will be positioned outside the RF coil. Because the field strength decays rapidly with distance from the coil surface [41], most of the published experiments were performed with samples positioned within a radius of the RF coil used. The field drop off can be roughly estimated with the following equation [18]:

$$B = \frac{\mu_0 I}{2} \frac{r^2}{(r^2 + x^2)^{3/2}} \quad (4.3)$$

The above equation describes the axial field strength as a function of the distance  $x$  from the plane of the loop for a circular loop of current  $I$  with radius  $r$ . For small  $x$ , the equation roughly scales as  $1/r$ . One can also see the advantages of using a small RF coil. By downsizing the coil, one could, in principle, generate a larger field with a smaller current. Since the power dissipation goes as  $I^2$ , less heating could be achieved with smaller coils. Lower current also means lower voltage across the tank circuit. This in turn would allow the use of lower voltage rated tuning and matching capacitors for a given field. Figure 4.8 shows the result of the conventional NMR  $T_1$  measurement on the deuterium oxide sample in the Cryomagnetics NMR magnet. The data was fitted well fitted well to an exponential to correctly describe the exponential recovery law of the magnetization, providing the value of  $T_1 = 0.33$  s at 52.716 MHz for this D<sub>2</sub>O specimen.

From measuring the  $\pi$ -pulse length, the strength of  $B_1$  field from a centimeter-size NMR coil was calculated to be  $\sim 12$  G. It is advantageous to look for the length of the  $\pi$ -pulse instead of a  $\pi/2$ -pulse since around the

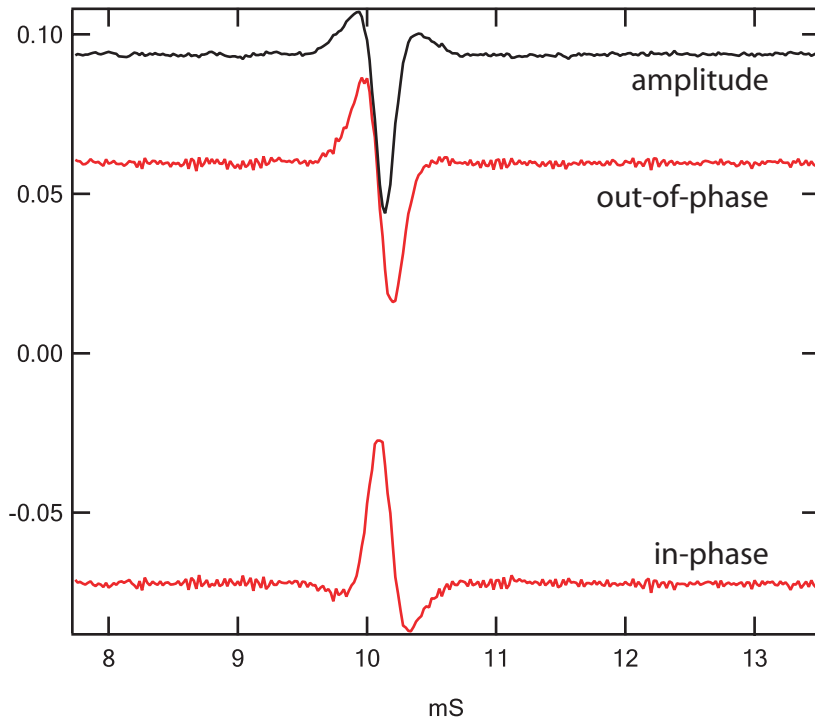


Figure 4.7: An example of a measured spin echo from a sample of  $D_2O$ . It is measured with a millimeter-size coil.

$\pi/2$ -pulse length, the change in the NMR echo amplitude is rather small as a function of the pulse length; it is difficult to pin-point the exact length of a  $\pi/2$ -pulse. However, the length of the  $\pi$ -pulse can be more precisely determined because the point of zero crossing is much more sensitive to changes in pulse length. This is one reason why we measured the length of a  $\pi$ -pulse and divided the result by two to obtain the length of the  $\pi/2$ -pulse.

The same experiment was performed with a smaller millimeter-size RF coil installed in the MRFM probe. If we cannot see a NMR signal in the probe, it would mean that the signal-to-noise ratio for the small coil is too small or

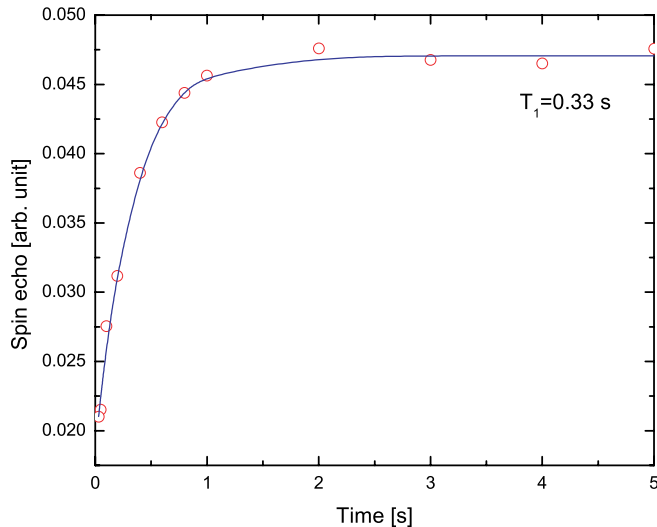


Figure 4.8:  $T_1$  measurement from the conventional NMR experiment with a millimeter-size coil. The standard saturation recovery with a  $\pi/2 - \tau - \pi$  pulse sequence was used for measurement as discussed in Chapter 2. For a comparison of data, see result from [11]. The solid line is an exponential fit to the data.

there is something that creates a field inhomogeneity at the RF coil location. Fortunately, we successfully detected a deuterium NMR signal with the small RF coil. The length of a  $\pi/2$ -pulse was determined to be  $\sim 4.25 \mu\text{s}$ . This corresponds to  $B_1 \sim 80 \text{ G}$ . Here we could verify that the field strength increased with a smaller coil volume as predicted by (3.7). At this point, it would be helpful to know how much power was delivered to the tank circuit by the RF amplifier. Past group members noticed that the ENI 5100L RF amplifier used in this experiment had an incorrect gain [33]. The amplifier showed only 41.1 dB gain instead of the nominal 50 dB gain in power. Since every 3 dB loss corresponds to an approximate power loss by a factor of 2, the loss of 9 dB

would reduce the maximum output of the amplifier to be about 12.5 watts.<sup>7</sup> We believe that the calculated  $B_1$  field strength was achieved with about 12 watts of power sent to the tank circuit. Therefore, we concluded that the sub-millimeter-size RF coil used in a force-detected MRFM experiment would generate a sufficiently large  $B_1$  field.

Initially, we had utilized the gating feature of the RF amplifier. This gating function, in principle, should disable all 8 transistor amplifier stages so that the output is less noisy compared to when the amplifiers are on. Hence, we not only used a RF switch to generate RF pulses but also gated the RF amplifier with the same control pulse programmer pulse that controlled the RF switch. This means that at the beginning of a cyclic adiabatic inversion sequence, the amplifier was gated to be on. It turned out that our ENI 5100L amplifier showed an output ringing that lasted about 100  $\mu$ s. The output ringing seemed entirely caused by a TTL/CMOS logic signal that turned the amplifier stages on or off. The ringing showed up whenever there was a logic level transition at the gating input of the amplifier regardless of whether there was an input to the amplifier or not. This meant that even without anything connected to the amplifier input, the output ringing could be generated by simply gating the amplifier on or off. This can be detrimental to the cyclic adiabatic inversion if this ringing has a significant frequency component at

---

<sup>7</sup>The ENI 5100L amplifier has 8 identical inner amplifier stages. A preamplified input signal is split into 8 equal parts and separately fed to 8 amplifier stages. The amplified signals are then added by the power combiner to produce a gain of 50 dB. It seems that one or more of these stages are malfunctioning or damaged.

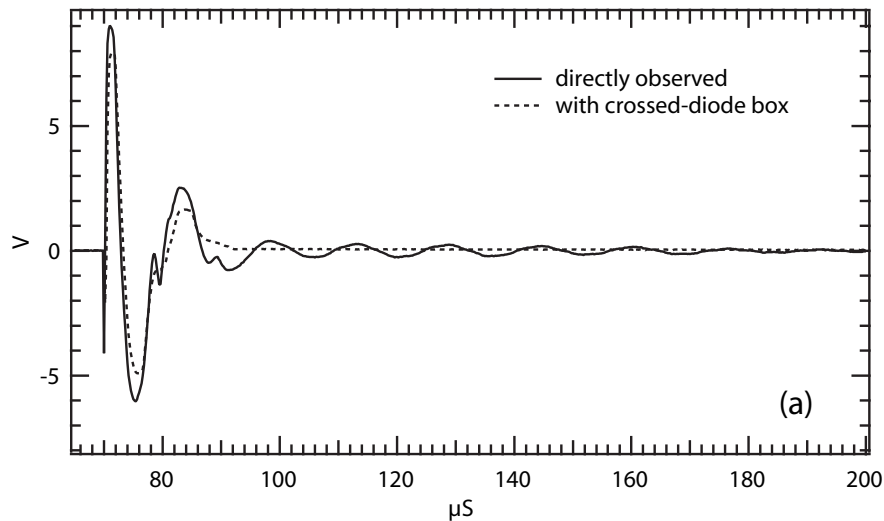


Figure 4.9: Ringing in the ENI 5100L RF amplifier output. This ringing lasts for several tens of  $\mu\text{s}$ . From [11]. We have observed the identical ringing.

the Larmor frequency of the nuclei under investigation. Our current setup does not utilize the gating function of the RF amplifier. The amplifier noise present at the output is not a big concern as in a conventional NMR where even small noise can swamp the actual NMR signal or overload the preamplifier. In a force-detected NMR, the signal is read out with an optical interferometer which is insensitive to the RF amplifier output noise.<sup>8</sup>

After the successful conventional NMR experiment, we went back to the force-detected NMR experiment. However, we were not able to observe any spin-induced signal. We then set out to investigate the so called spurious

---

<sup>8</sup>If there is a significant RF-cantilever coupling, the RF noise from the amplifier output can in principle cause or enhance the amplitude noise of the cantilever. Any increase in the noise level is not due to an increase in the interferometer noise but due to an actual increase in the cantilever noise. The optical detection is superior to the inductive detection in the sense that the transmitter-detector(preamplifier) isolation is much better.

RF-induced excitations. They had been known to exist and there were many attempts to suppress or eliminate them [4, 9, 28, 31]. In particular, a two-step phase cycling protocol in [9, 28] seems to be an elegant solution to eliminate the contribution from a spurious excitation to the detected signal from the raw data during the MRFM readout stage. A more detailed description of the technique will be given in the next chapter. Presently, there is no clear explanation for the spurious phase coherent excitation of a cantilever by a frequency modulated RF field. This effect is exclusively caused by the FM of the RF carrier. If there is no FM, there is no spurious excitation. The generally accepted explanation of this phenomenon is as follows. The tuning of a tank circuit is frequency dependent. Usually, a tank circuit in a MRFM experiment is tuned to the resonant (Larmor) frequency of the nuclei under investigation. But the transmitted RF wave to the tank circuit will be impedance-matched or mismatched as a function of time when the carrier is frequency modulated. The resonance curve will peak at the tuned frequency and decrease as the frequency moves away from the tuned frequency. Because of this frequency dependent nature of resonance phenomenon, the power of the transmitted RF gets amplitude modulated (AM) as well when there is frequency modulation (FM). This mistuning will not be very significant because the FM depth is on the order of a couple of hundred kHz or less and the tuned center frequency is on the order of a hundred MHz. However, because of the extreme sensitivity of the cantilever used in the experiment, even a small amplitude modulation of a RF carrier can couple to the cantilever motion electrostatically or by



other means. The amplitude response of a cantilever therefore depends on the details of the experimental setup and is unique to each microscope. Despite such peculiarities, there are a couple of common qualitative behaviors. First, it seems that the amplitude of a spurious excitation scales linearly with RF power [31, 33]. However, as shown in Figure 4.10, our data showed a non-linear be-

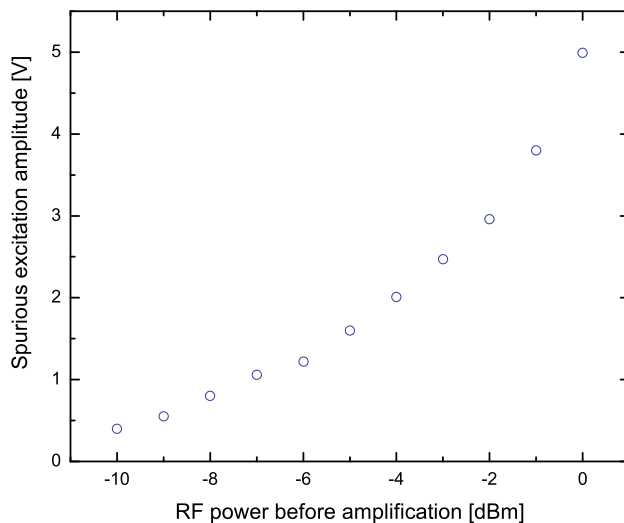


Figure 4.10: Dependence of spurious excitation on RF input power. The ENI 5100L RF amplifier was used to obtain this result. Note the non-linearity as opposed to a linear behavior claimed by others [31, 33].

havior. It could be argued that at low power a linear response is observed, but the overall trend clearly showed a non-linear behavior. We initially attributed this observation to the apparent RF amplifier gain problem, and no further investigation attempt was made. This turned out to be a big mistake because we later discovered that the RF amplifier had problems truthfully amplifying frequency modulated signals. The amplifier added an amplitude modulation to the amplified signal although the input signal does not have any amplitude

modulation. When we compared the level spurious excitation caused by two RF amplifiers (ENI 5100L and ENI 406L), the ENI 5100L caused a bigger spurious response from the cantilever at the same power level. The power modulation resulting from the amplitude modulation seemed to enhance the unwanted excitation. The ENI 5100L RF amplifier, however, did correctly amplify an unmodulated signal. This allowed us to do a conventional NMR previously since only a single frequency RF carrier was needed for a successful experiment.

We then switched to the ENI 406L amplifier that could deliver about 5 watts to a  $50 \Omega$  load. But since its operating frequency is limited to 250 MHz, we could not use  $(\text{NH}_4)_2\text{SO}_4$  as our sample. Our solution was to purchase deuterated ammonium sulfate  $(\text{ND}_4)_2\text{SO}_4$ . Its  $T_1$  at room temperature was on the order of 1 s, long enough for the cyclic adiabatic inversion sequence [26]. The expected signal when compared to  $^1\text{H}$  NMR signal from  $(\text{NH}_4)_2\text{SO}_4$  would be smaller since the NMR sensitivity scales as  $\gamma$ , but we had performed conventional NMR experiments on deuterium nuclei successfully in the past. But we still had a concern about the effect of the small gyromagnetic constant ( $\gamma = 6.536 \text{ MHz}$ ) on the adiabatic condition and the thickness of a resonant slice. Since the adiabatic condition is given by (2.33), the allowed FM depth  $\Omega$  would decrease with the smaller  $\gamma$ . Then a smaller value of  $\Omega$  would result in thinner resonant slice decreasing the signal strength. For example, if  $f_{\text{osc}} = 1.2 \text{ kHz}$  and  $B_1 = 15 \text{ G}$ , the right hand side of (2.33) will be  $\sim 20 \text{ kHz}$ . This means that we can probably safely choose  $\Omega = 10 \text{ kHz}$ . The resonant slice

thickness for  $\nabla B = 250$  T/m is then about  $12 \mu\text{m}$ . Given the fact that the NMR sensitivity of deuterium is smaller than that of hydrogen, this resonant slice may not contain enough spins for the cantilevers used for detection whose spring constants are on the order of  $10^{-2}$  N/m.<sup>9</sup>

Despite many attempts, we were not able to observe a deuterium NMR induced signal. We believe that the smaller receptivity coupled with the smaller gyromagnetic ratio prevented a successful detection with the cantilever used in the experiment. The equilibrium magnetization per unit volume is given by the Curie law

$$M_0 = \frac{2\rho(\gamma_D\hbar)^2 B_0}{3k_B T} \quad (4.4)$$

where  $\rho$  is the nuclear number density and  $\gamma_D$  is the deuterium gyromagnetic ratio. Given the sample's lateral dimensions shown in Figure 4.4 and the resonant slice thickness of  $12 \mu\text{m}$ , the net magnetization at  $8.2$  T<sup>10</sup> and  $300$  K is  $3.54 \times 10^{-17}$  J/T. Then the net force induced on the cantilever is  $8.87 \times 10^{-15}$  N. The minimum detectable force given by equation (1.1) for the cantilever<sup>11</sup> used is  $F_{\text{min}} = 6.6 \times 10^{-15}$  N. This is the thermally limited sensitivity, and our measurement noise floor is about 2 times higher because of an environmental vibration. We were expecting a better SNR by performing signal averaging. When designing a future experiment, we would like to have a signal-to-noise

---

<sup>9</sup>Of course the lateral dimension of the sample must be considered in order to calculate the resonant sample volume.

<sup>10</sup>At a  $1$  mm sample-magnet distance, the magnetic field from the gradient producing magnet is  $0.16$  T. Hence, the total field is  $8.07 + 0.16 = 8.23$  T. The magnetic field gradient at the same distance is  $250$  T/m.

<sup>11</sup> $\omega_{\text{osc}} = 2\pi(1.2)$  kHz,  $Q = 1000$ ,  $\Delta\nu = 1$  Hz, and  $k = 0.02$  N/m.

(SNR) ratio of 10 or more because there can be factors that would lower the measured SNR including noise in electronics, mechanical vibrational noise, temperature instability, etc. Therefore, we must come up with a more favorable experiment where we would get a bigger SNR. In the next chapter, I will discuss what directions to take for a successful detection of force-detected NMR.

# Chapter 5

## Future Directions

### 5.1 Modifications to the Experimental Setup

There are several areas that can be changed or modified to improve our chance of detecting a spin-induced signal.

First, we now have a variable field superconducting magnet that can be used to find the resonant field for nuclear spins a little more conveniently. So far, our Cryomagnetics' NMR magnet has generated a fixed field of 8.07 T.<sup>1</sup> In order to scan for the resonant field, we have been moving the gradient-producing magnet toward or away from the sample. Although we have calibrated and verified the movement of the piezoelectric positioner, the ability to vary the strength of magnetic field without anything moving will allow a more stable measurement. The superconducting magnet has been set up, and the central field location and the field strength have been verified.

Second, we have recently purchased another ENI 5100L RF amplifier that was tested to function correctly. This replacement amplifier will eliminate a possible source of problems in future experiments.

---

<sup>1</sup>The NMR magnet has shim coils to maximize the field homogeneity over a large volume. Although the magnetic field can be changed to a new value, we must re-set the shim coils to maintain the high level of field homogeneity.

Third, we should return to ordinary ammonium sulfate  $(\text{NH}_4)_2\text{SO}_4$  sample since we have a new RF amplifier that allows us to look for a signal at any frequency within 5 to 400 MHz.  $^1\text{H}$  nuclei will induce a bigger force on a cantilever than deuterium. Also, the FM depth can be made larger because of its larger gyromagnetic ratio. A bigger FM depth results in a thicker resonant slice. Hence, we expect a bigger SNR with  $(\text{NH}_4)_2\text{SO}_4$ . The resonant slice thickness can be decreased to a smaller value to estimate the sensitivity of the microscope once a signal is successfully detected.

A multifunction DAQ from National Instruments<sup>2</sup> has been incorporated in the setup. This simplifies our experiment in the sense that the DAQ can generate not only the FM voltage pattern but also the RF switch control pulse and a TTL-compatible waveform synchronous with the FM voltage pattern for the lock-in amplifier's reference input. A Labview-based PID<sup>3</sup> program can also be incorporated so that a more flexible feedback parameter control such as proportional and integral gains and input and output filtering can be achieved.

## 5.2 Phase Cycling

In this section, I would like to discuss a recent method [9, 28] that can be applied to MRFM in order to suppress or eliminate the spurious excitation contribution to the spin-induced signal at the data-taking stage. The idea be-

---

<sup>2</sup>Model PCI-6711

<sup>3</sup>Proportional, integrative, and derivative control

hind the technique comes from the phase cycling method used in a conventional NMR experiment to eliminate spurious signals. The two-step phase cycling is

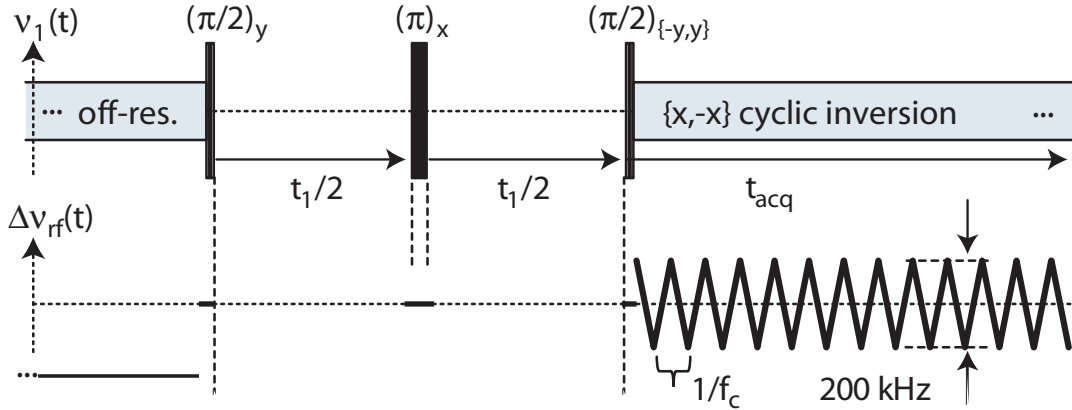


Figure 5.1: Two-step phase cycling from [9].

described in Figure 5.1. During the off-resonance period, the magnetization is aligned along the  $+z$  axis. The first  $\pi/2$ -pulse tips the magnetization onto the  $x$  axis. The  $\pi$ -pulse then forms an echo. This echo formed at time  $t_1$  is tipped either onto  $+z$  axis or  $-z$  axis depending on the phase of the second  $\pi/2$  pulse. The cyclic adiabatic inversion readout sequence that follows the second  $\pi/2$ -pulse is phase-conjugated every measurement cycle like the second  $\pi/2$ -pulse.

Let's follow what happens to the magnetization and the effective field during the first measurement sequence. After the last  $\pi/2$ -pulse, the magnetization is aligned along the  $+z$  axis. Because of the particular FM waveform used for the cyclic adiabatic inversion readout the effective field starts along the  $-z$  axis and approaches the  $+x$  axis adiabatically. Since the magnetization

was aligned along the  $+z$  axis, the magnetization and the effective field are anti-parallel. This means that the FM-induced spurious excitation and the spin-induced signals will have an opposite phase. The second of the two-step

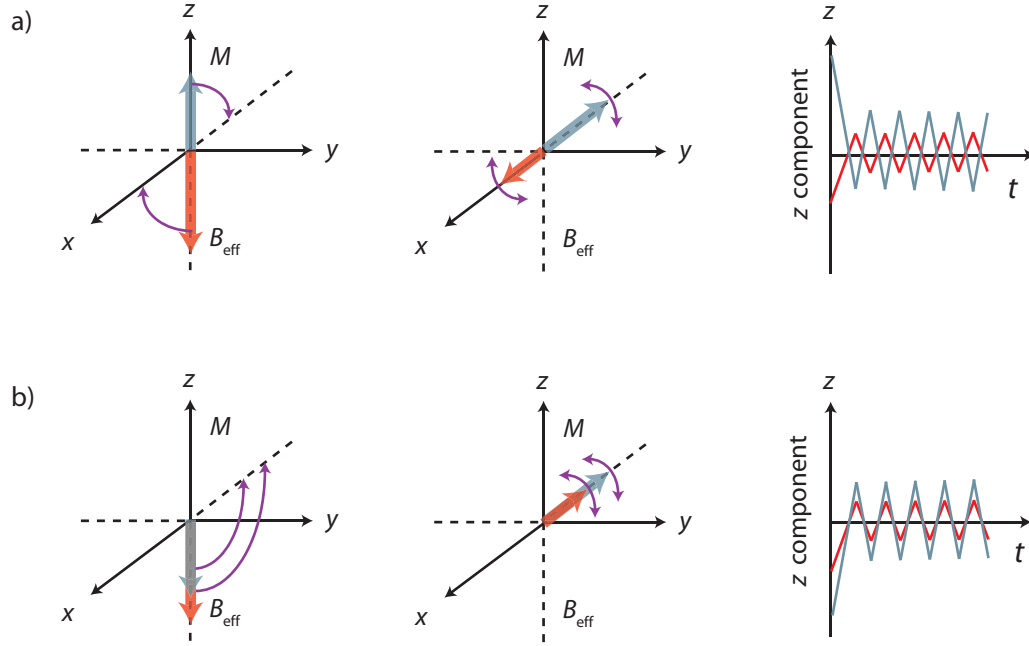


Figure 5.2: a) First of the two readout sequence in the two-step phase cycling.  $B_{\text{eff}}$  and  $M$  are aligned anti-parallel initially. See text for the explanation. The cyclic adiabatic inversion sequence with the  $x$ -phase RF brings  $B_{\text{eff}}$  onto the  $x$  axis. The resulting  $z$  components are graphically shown. b) Second of the two readout sequence. After the last  $\pi/2$ -pulse,  $M$  and  $B_{\text{eff}}$  are aligned parallel. The cyclic adiabatic inversion sequence with the  $-x$ -phase RF brings both  $M$  and  $B_{\text{eff}}$  onto  $-x$  axis. The resulting  $z$  components are graphically shown.

phase cycling is described next. The last  $\pi/2$ -pulse tips the magnetization  $M$  onto the  $-z$  axis. Hence for the given FM waveform, both  $M$  and  $B_{\text{eff}}$  are aligned parallel. Then the cyclic adiabatic inversion readout sequence with



$-x$  will bring both  $M$  and  $B_{\text{eff}}$  onto  $-x$  axis. This means there is no phase difference between  $M$  and  $B_{\text{eff}}$ . Therefore, by a proper choice of averaging,<sup>4</sup> one can in principle eliminate the spurious excitation due to the frequency modulated RF.<sup>5</sup> This technique will allow us to subtract the contribution to the raw signal from the spurious excitation, simplifying data processing at a later time. The strength of a spurious excitation will not change significantly during the two-step phase cycling. But if one measures the signal containing both the spin-induced part and the spurious excitation for the entire experiment, the strength of the spurious excitation may drift significantly over time. This makes the later data processing much more difficult or even impossible. The fact that we do not need to keep track of the spurious excitation level will greatly improve the chance of a successful detection.

However, the above mentioned phase cycling technique assumes the knowledge of the lengths of  $\pi/2$  and  $\pi$  pulses. In a more typical circumstance, the experimenter would not know the values of those pulse lengths. It is conceptually easy to imagine that the phase cycling technique will give the same result if one fixes the direction of the magnetization and switches the initial direction of  $B_{\text{eff}}$ . This change is significant in that the use of  $\pi/2$  and  $\pi$  pulses is not needed. This modified phase cycling should be utilized in future experiments.

---

<sup>4</sup>It must be an even-number averaging.

<sup>5</sup>Of course this assumes that the spurious excitation level does not change during averaging.

## Appendices

## Appendix A

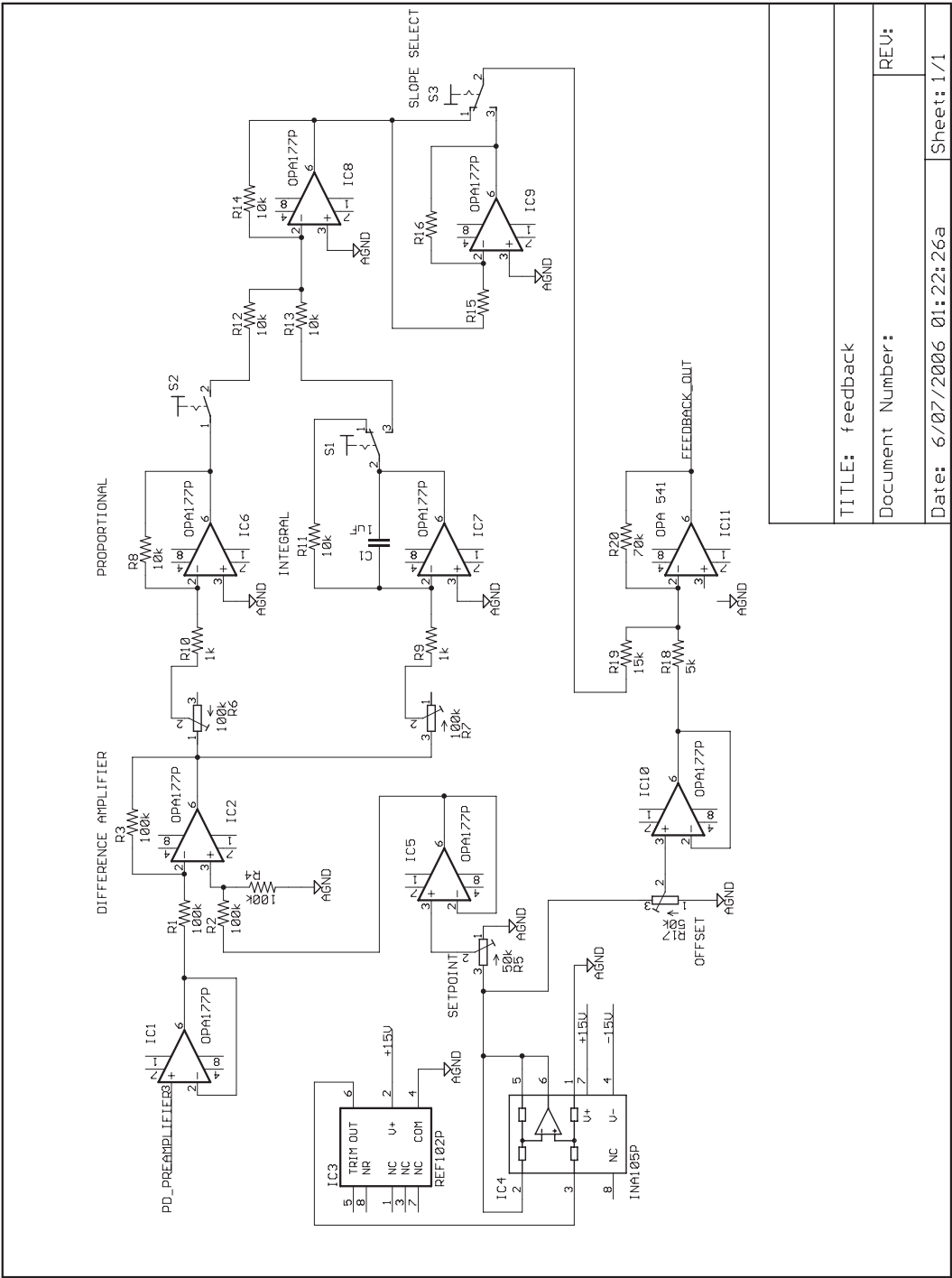
### Feedback Electronics

The fiber optic interferometer, as discussed in 3.2, must operate at the mid-point of the interference fringe. This means that the interferometer cavity length formed by the cleaved face of the optical fiber and the surface of a cantilever must be maintained constant. During an experiment the cavity length can change and drift over time due to various reasons such as temperature gradient, laser wavelength fluctuation, temperature drift, external mechanical vibrations, etc. However, the drift related to temperature is slow so that even a moderate ( $\leq 1000$  Hz) feedback works quite well. External mechanical vibrations can be isolated to an acceptable level by a careful design. Figure A.1 shows the schematic of the feedback circuit used in the experiment.<sup>1</sup> It is a typical analog feedback circuit used in many applications such as heater temperature control, motor speed control, etc. Here is the operational aspects of the circuit.

1. The setpoint for the feedback circuit to lock onto must be set. This is usually the mid-point of the interference fringe. Using the offset potentiometer, first adjust the interferometer output level to the mid-point of

---

<sup>1</sup>See [17] for more discussion about the feedback circuit.



TITLE: feedback
Document Number:
Date: 6/07/2006 01:22:26a
Sheet: 1/1

Figure A.1: Interferometer feedback circuit.

the fringe. The offset is used to avoid a large initial jump in the feedback output if the setpoint is much different from the current interferometer output. Note the slope of the fringe for a later adjustment. After moving to the center of the fringe, adjust the setpoint potentiometer. This can be achieved by adjusting the potentiometer until the error output (this is the output of the difference amplifier) is zero.

2. The feedback slope polarity switch should be set to the appropriate position, based on the slope of the fringe from the previous step.
3. The integrator feedback can be turned on. The feedback bandwidth can be varied by adjusting the integrator gain potentiometer.
4. The proportional feedback can be turned on. The proportional feedback gain can be varied by the potentiometer on the front panel.
5. Check for the proper operation of the feedback circuit. The output of the circuit should not have a initial jump. If the slope is incorrectly chosen, the feedback output will jump to a new value. This happens because the circuit will lock onto the center of the next fringe with the correct slope. If a wrong slope was chosen, the slope can be reset and the process repeated.

This kind of feedback control is inherently manual in the sense that if the interference fringe levels change, the new setpoint must be calculated used to re-set the feedback. Also if the interferometer drift causes the feedback output

to drift in one direction and saturate, the feedback must be disengaged and re-set. However, it was very rare that the interferometer fringe level changed significantly or that the feedback output saturated.

A more elaborate feedback scheme has been used in [32, 51]. It can be shown that the second harmonic component of the interferometer at the fringe center is zero. This fact can be used to automatically center the feedback control by continuously monitoring the second harmonic with a lock-in amplifier. In other words, if the oscillator frequency is  $\omega_0$ , a lock-in amplifier's reference is set to measure  $2\omega_0$  signal.<sup>2</sup> The feedback is designed to actively follow the location where the second harmonic signal is zero. This scheme allows no further user control once the feedback is engaged. The drawback for this scheme is the use of one more lock-in amplifier since one needs one lock-in amplifier for the signal detection at  $\omega_0$ . If there is a spare lock-in amplifier, this method can be readily applied to our setup without a major modification. However, for some types of fluctuations, such as laser intensity fluctuations, the simpler "DC level" feedback may provide greater position stability than the "fringe center" feedback.

---

<sup>2</sup>This is simply done utilizing the harmonic reference function of the lock-in amplifier. Although the reference input is at  $\omega_0$ , a lock-in amplifier can be set to measure the signal component at  $2\omega_0$  without any other extra hardware.

## Appendix B

### Inertial Positioner Driver Electronics

Piezoelectrically driven inertial positioners utilize piezoelectric stacks to amplify the motion. Typically, piezoelectric stacks are polar. This means that the voltage applied to two electrical leads to a stack must have the proper sign of the potential difference. The piezoelectric stacks used in the current positioners<sup>1</sup> have red and black leads to clarify the required polarity. For these piezoelectric stacks the red lead must be positive with respect to the black lead. Hence, for convenience, the black lead is usually grounded and only a positive voltage is applied to the red lead. The maximum driving voltage is 150 V. However, when driven at such a high voltage, the lifetime of the piezoelectric stacks shortens considerably faster. The manufacturer recommended a driving voltage below 100 V. In many cases, we do not need to drive the piezoelectric stacks with more than 20 V.

One other characteristic of a piezoelectric stack to consider in building the driver electronics is the capacitance of the stack. The nominal capacitance of AE0505D08 is 0.75  $\mu\text{F}$ . This is a much bigger capacitance than that of piezoelectric tubes (typically on the order of few tens of nF) used in SPM

---

<sup>1</sup>NEC Tokin model # AE0505D08

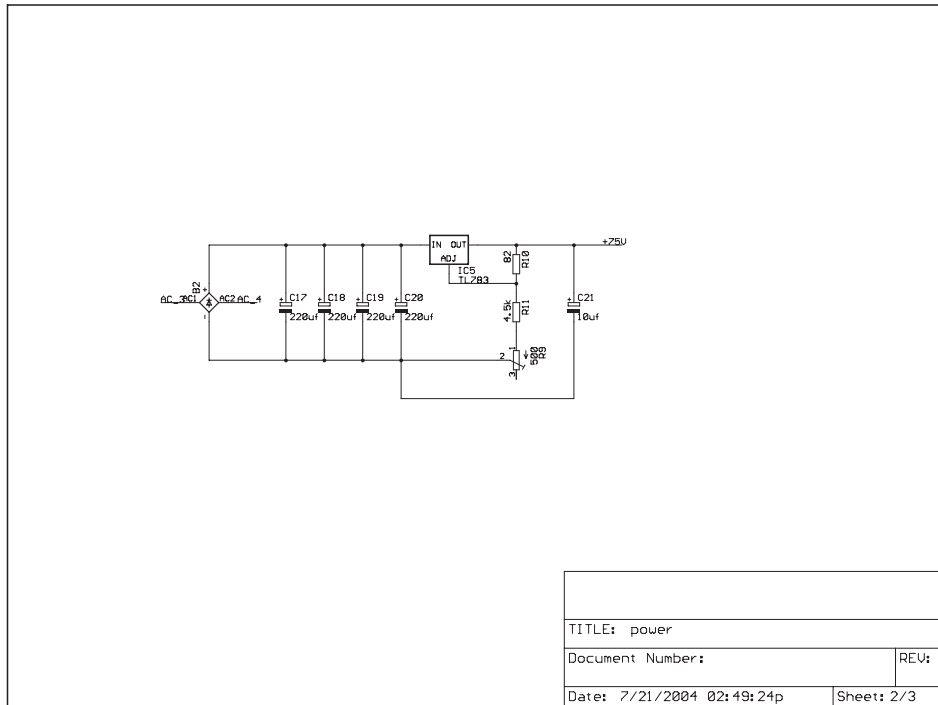


Figure B.1: 75 V power supply using a TL783 linear regulator from Texas Instruments. Proper heat sinking is required for stable operation. For more information, refer to the datasheet for the TL783 from Texas Instruments.

(Scanning Probe Microscopy) instruments.

Figure B.1 shows the 75 V power supply for the high voltage amplifiers. A TL783 chip from Texas Instruments is employed to supply a linearly regulated DC power from unregulated DC voltage. Since OPA541<sup>2</sup> can be supplied up to 80 V differential power, +75 V and -5 V were chosen. Although a single supply design can be employed, an asymmetrical supply design will be more

<sup>2</sup>OPA541 was chosen for driving piezoelectric stacks because of its low price and current handling capability. Equivalent power operational amplifiers from Apex Microtechnology costs about twice as much. However, if one needs higher output voltage (i.e., bigger than 70 V), PA03 or PA04 from Apex Microtechnology should be considered.



predictable and stabler in many cases. Because the depolarization voltage on similar piezoelectric stacks were found to be  $\sim 40$  V [17],  $-5$  V output from the high voltage amplifier should not result in a damage to the stacks used in the positioners.<sup>3</sup>

Low voltage supplies ( $\pm 15$  V and  $\pm 5$  V) are obtained from simple 7815, 7805, 7915, and 7905 series linear regulators. See Figure B.2 for a generic schematics.

A sawtooth waveform is generated by a digital-to-analog converter. TLC7524 from Texas Instruments is used to convert 8-bit digital numbers to analog voltages in the range of 0 to 5 V.<sup>4</sup> A counter is incremented by one in a loop. Depending on the execution time of this loop, one can effectively control the frequency of the sawtooth waveform. An example of a simple PIC assembly will be shown later. For more information about the assembly commands, refer to datasheets for PIC micro-controllers. For a ramp-up waveform, the counter is incremented, while for a ramp-down waveform the counter is decremented. Figure B.3 shows how TLC7524 is connected to a PIC16F877A micro-controller<sup>5</sup>. In this design, two separate micro-controllers are used to produce ramp-up and ramp-down waveforms. However, for the current design, only one micro-controller is used to generate either waveform. By controlling

---

<sup>3</sup>OPA541 cannot swing all the way to the supply voltages. Hence the most negative voltage from the amplifier will be few volts higher, i.e. closer to 0 V.

<sup>4</sup>MX7524 is a pin-to-pin compatible DAC from Maxim Semiconductors.

<sup>5</sup>These micro-controllers have flash-based memory which can be erase and re-written electrically. Non-flash versions, i.e. EEPROM versions, must be erased by a exposure to UV light prior to re-programming.

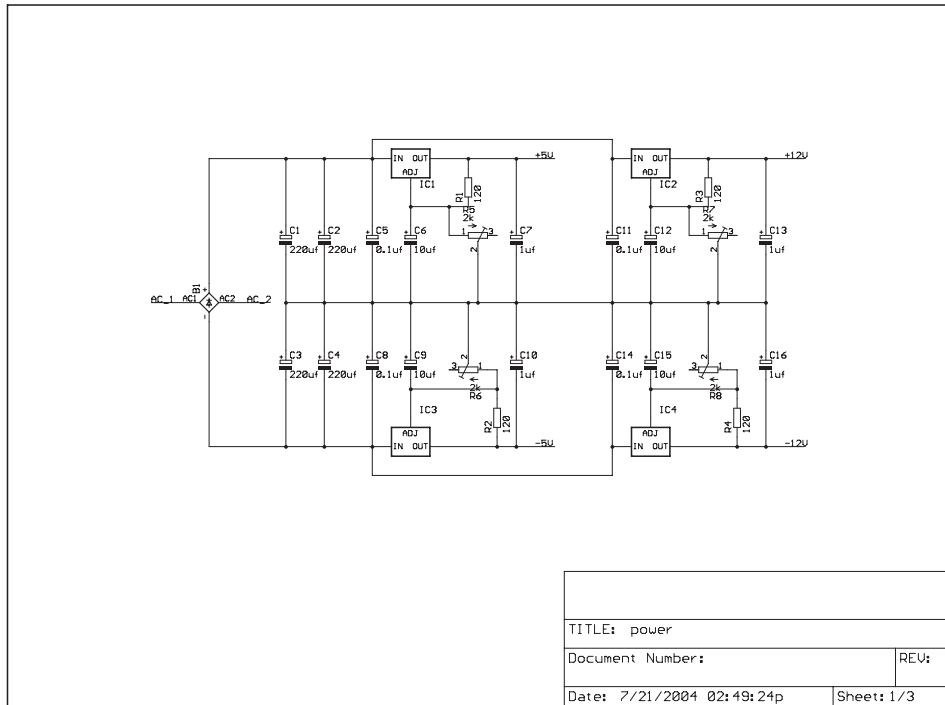
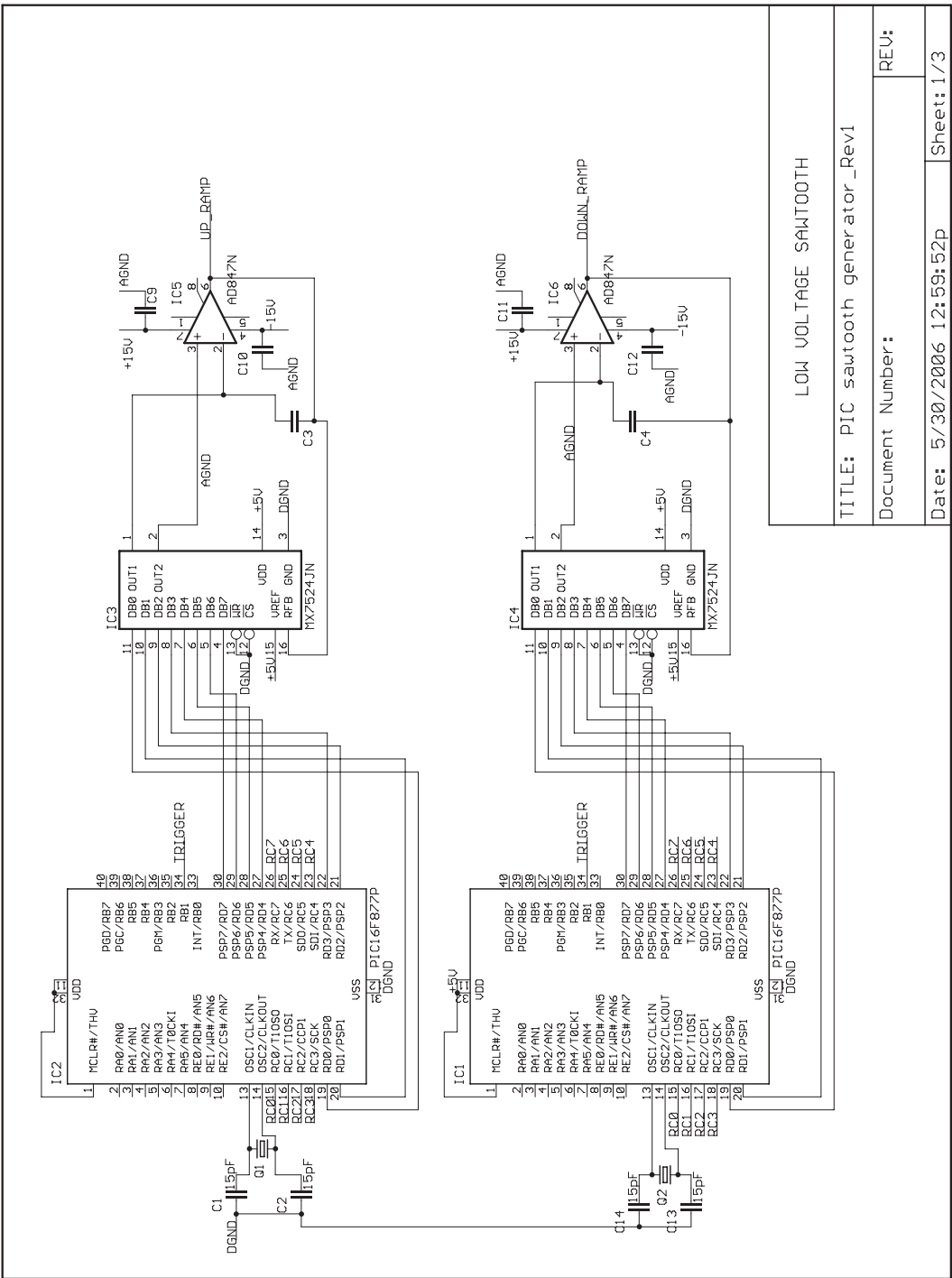


Figure B.2: Low Voltage Power Supplies. The design can be used in any laboratory DC power application. Proper heat sinking is required for regulators.

the logic state of one I/O pin, the software decides to ramp-up or ramp-down. Hence, a switch on the front panel of the piezo driver is used to select the direction of the sawtooth waveform. Since a mechanical switch is used to drive a digital line to high or low, one must use a mechanical contact debouncing circuit. A simple debounce circuit using a couple of inverters, a resistor, and a capacitor can be utilized, although MC14490 chips have been used in the current design.<sup>6</sup>

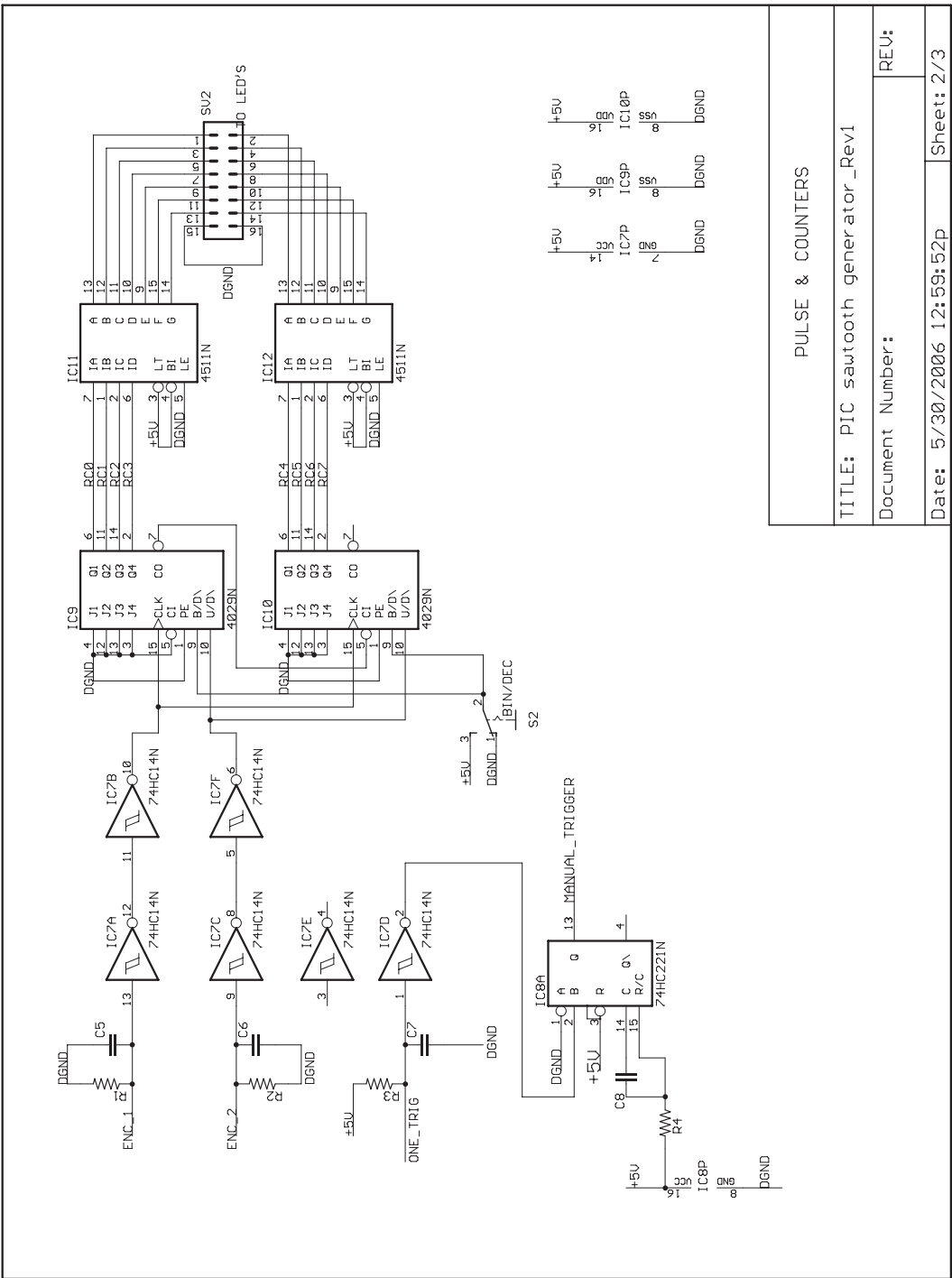
Figure B.4 shows the frequency and manual pulse generation control.

<sup>6</sup>MC14490, On Semiconductor.



LOW VOLTAGE SAWTOOTH	
TITLE: PIC sawtooth generator_Rev1	
Document Number:	REV:
Date: 5/30/2006 12:59:52p	Sheet: 1/3

Figure B.3: DAC Connection diagram to PIC micro-controller.



PULSE & COUNTERS	
TITLE: PIC sawtooth generator_Rev1	
Document Number:	REV:
Date: 5/30/2006 12:59:52p	Sheet: 2/3

Figure B.4: Sawtooth waveform controls.

Frequency is controlled by turning an encoder. Clockwise turning increments the delay between successive loop execution, thus lowering frequency. Counterclockwise turning has the opposite effect. The sawtooth waveform is generated continuously as long as a chosen digital I/O pin is high. After the generation of one sawtooth, the program checks whether that I/O pin is still high. If the pin is high, the program generate one more sawtooth. If not, the micro-controller waits until the pin returns high. Hence, by sending a high pulse shorter than the period of the sawtooth waveform, only one sawtooth waveform is generated. The push button switch on the front panel does this job. More flexibility in the number of sawtooth waves generated can be attained if one constructs an N-pulse generator<sup>7</sup>, the output of such a unit can directly drive the proper I/O pin of the micro-controller for a more complete, automated control.

---

<sup>7</sup>N number of pulses are generated by this unit. Each pulse should last shorter than the period of sawtooth (typically, on the order of few  $\mu s$  is good enough), while pulses should be separated by more than the period of the sawtooth waveform.

## Appendix C

### Frequency Modulation Electronics

For frequency modulating an RF carrier, we utilize the DC FM function of the RF signal generator. In the DC FM mode, the frequency of the RF output is linearly deviated from the carrier frequency by the amount proportional to the DC voltage present in the modulation input terminal of the RF signal generator. The modulation depth<sup>1</sup> for our SML 01<sup>2</sup> RF signal generator is achieved with  $1 V_{\text{peak}}$ .<sup>3</sup> In order to generate the required voltage pattern, we utilize the following circuit in conjunction with a function generator.<sup>4</sup>

The voltage pattern can be divided into three parts: 1. approaching resonance, 2. modulation, and 3. departing from resonance. However, part 3 is often not necessary for measurement. Hence, the first two parts are incorporated in the electronics. The first part is generated from an exponentially growing voltage signal from  $-1 V$  to  $0 V$  with a user-set time constant as shown in a) of Figure C.2. The variable resistor R4 along with the internally fixed value capacitor C1 are responsible for setting the time constant. For

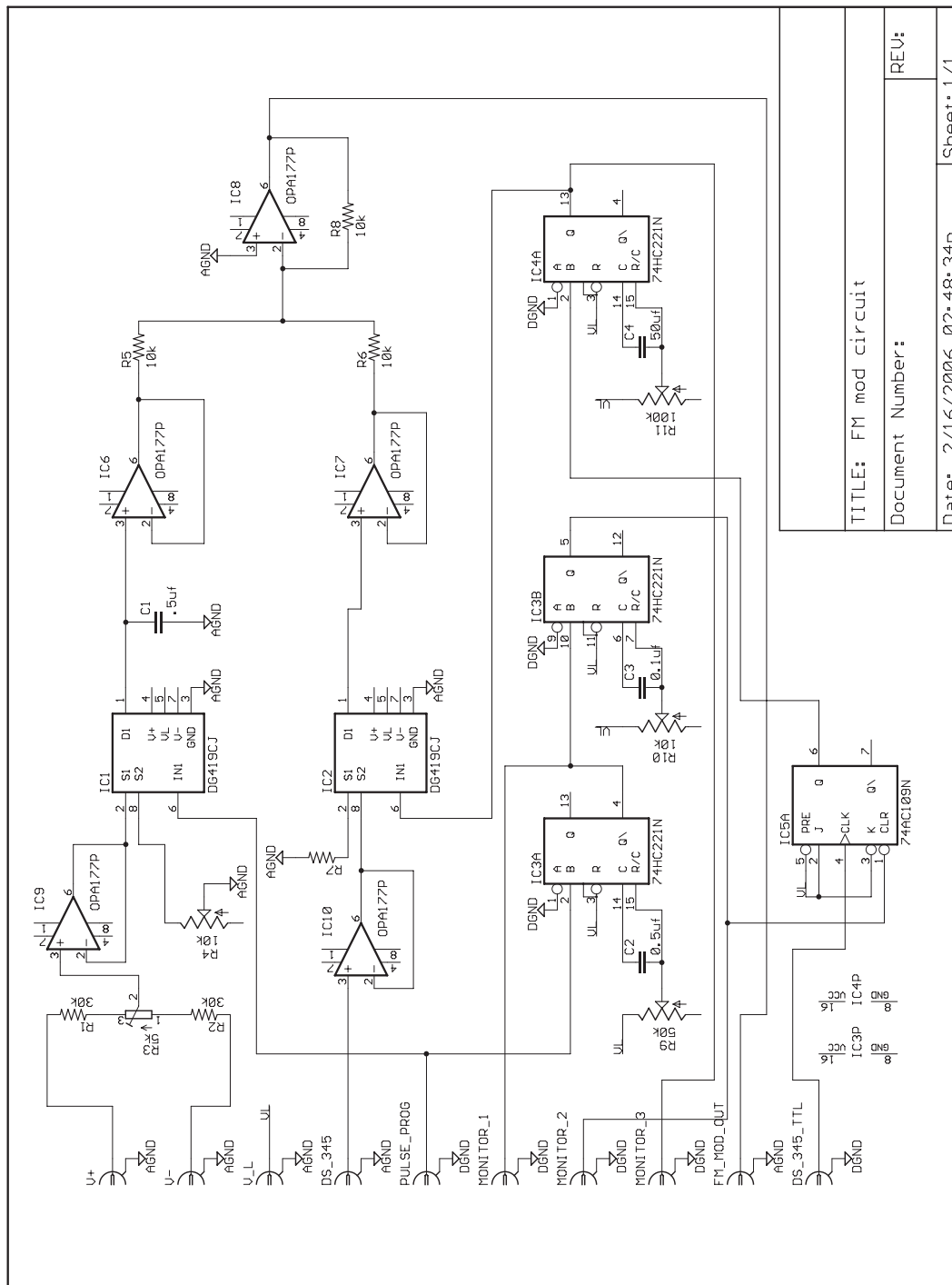
---

<sup>1</sup>It is the maximum frequency deviation from the carrier frequency. This can be adjusted for user's needs, but there is a limit for different carrier frequency bands. For details, one must refer to the operating manual of the RF signal generator in use.

<sup>2</sup>Rhode and Schwartz model SML 01

<sup>3</sup>For certain HP signal generators,  $1 V_{\text{rms}}$  is needed instead of  $1 V_{\text{peak}}$ .

<sup>4</sup>Stanford Research Systems model DS 345



TITLE: FM mod circuit
Document Number:
REV:
Date: 2/16/2006 02:48:34p
Sheet: 1/1

Figure C.1: Frequency modulation electronics responsible for correctly timing signal generator.

more flexibility, the variable resistor R3 can be used to vary the initial starting voltage before the growth or decay to 0 V. This way one can use the same electronics for other RF signal generators where  $1\text{ V}_{\text{rms}}$  is needed. The amount of growth or decay time can be controlled with the variable resistor R9. In about 5 time constants the voltage output from IC6 will be very close to zero. IC2 is an analog switch that allows the modulation waveform to pass through starting when it is 0 V and lasting for the pre-determined modulation time, controlled by the variable resistor R11. Since the waveform output of DS 345 is synchronized with the TTL output, the waveform crosses zero when there is a logic level transition as shown in c) of Figure C.2. Therefore, a sinusoidal modulation form can be used as well.



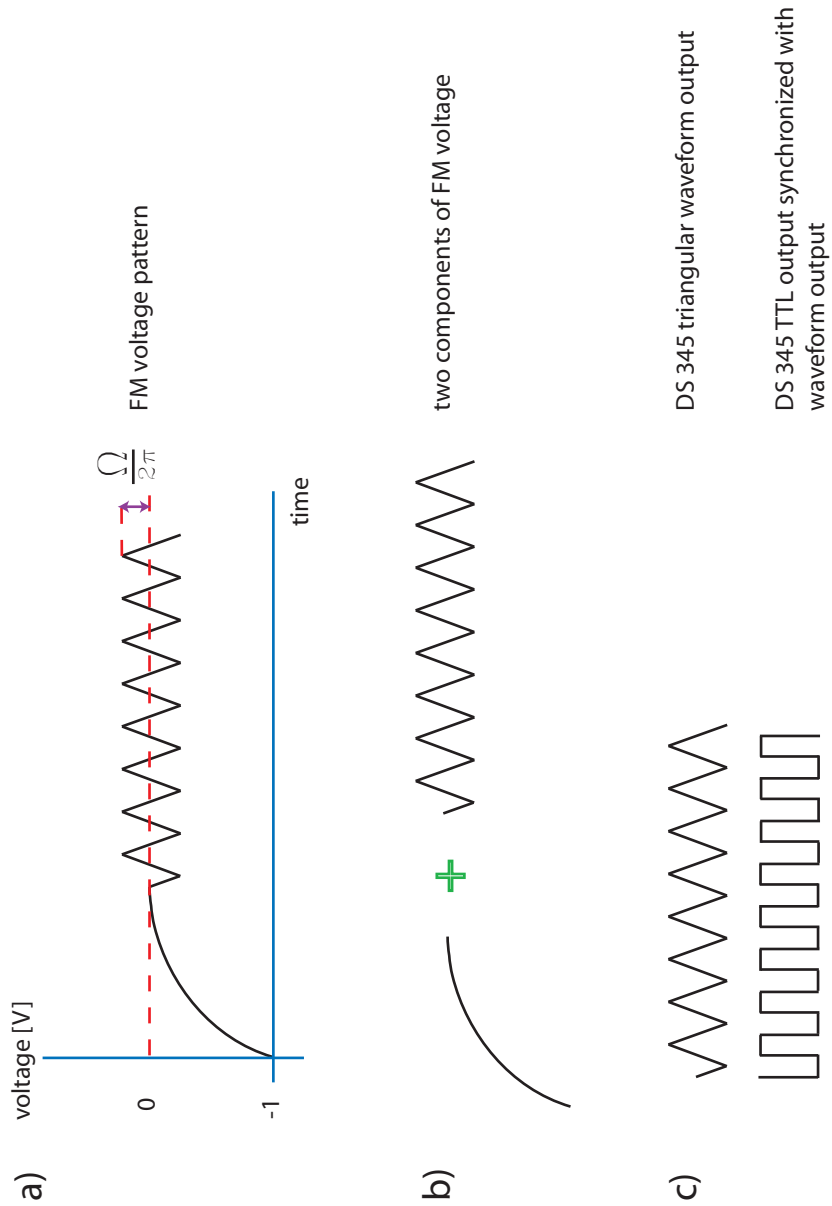


Figure C.2: An example of FM voltage signal generation. a) Triangular FM voltage used in MRFM. b) Two components of FM voltage. c) Waveform output in synchrony with TTL output

## Appendix D

### Errata in Oxford's HelioxVL $^3\text{He}$ Insert Manual

I would just like to point out that the chart that plots the loss against the frequency for the pre-installed flexible coaxial cables has the incorrect unit.<sup>1</sup> It should be noted that the frequency scale is in MHz, not GHz. Therefore, the installed cables cannot efficiently be used to transmit power at 350MHz<sup>2</sup> because of an unacceptably high loss level. In the present setup, a 50  $\Omega$  copper coaxial cable was installed. One of the SMB connector at the top of the probe is disconnected from the flexible stainless steel coaxial cable and connected to the copper coax. This custom installation will have a definite effect on the low temperature performance of the probe because of better thermal conduction of copper coaxial cable than stainless steel cable. However, by a careful heat sinking of the copper coaxial cable to the  $^4\text{He}$  pot, changes in the performance of the probe can be minimized.

---

<sup>1</sup>For correct specifications, see the datasheet for Lake Shore Cryotronics, Inc's Type SS cable.

<sup>2</sup>Our NMR magnet generates 8.07 T field at the center. For protons, this corresponds to 343.62 MHz

## Bibliography

- [1] <http://www.nr6ca.org/vf.html>.
- [2] Baierlein, R. *Newtonian Dynamics*. McGraw-Hill Inc., 1983.
- [3] Bruland, K.J., Dougherty, W.M., Garbini, J.L., Sidles, J.A., Chao, S.H. Force-detected magnetic resonance in a field gradient of 250000 t/m. *Appl. Phys. Lett.*, 73:3159–61, 1998.
- [4] Bruland, K.J., Krzystek, J., Garbini, J.L., Sidles, J.A. Anharmonic modulation for noise reduction in magnetic resonance force microscopy. *Rev. Sci. Instrum.*, 66:2853–6, 1995.
- [5] Butt, H.-J. and Jaschke, M. Calculation of thermal noise in atomic force microscopy. *Nanotechnology*, 6:1–7, 1995.
- [6] Chabot, M. *Force Detection of Nuclear Magnetic Resonance Using Double-torsional Micro-oscillators*. PhD thesis, The University of Texas at Austin, 2001.
- [7] Cobb, Jonathan. *Reversible DC Magnetization Measurements of the Superconducting Parameters and Their Anisotropies in the Randomly-Doped Cuprates and Prelude to the Magnetic Resonance Studies of T'-Phase Cuprate*. PhD thesis, University of Texas at Austin, 1995.

- [8] Conway, J.L. and Cotts, R.M. Circuit for a digital pulse programmer. *Rev. Sci. Instrum.*, 48:656, 1977.
- [9] Degen, C., Lin, Q., Hunkeler, A., Meier, U., Tomaselli, M, Meier, B. Microscale localized spectroscopy with a magnetic resonance force microscope. *Phys. Rev. Lett.*, 94:207601, 2005.
- [10] Dobosz, M., Usuda, T., Kurosawa, T. Methods for the calibration of vibration pick-ups by laser interferometry: I. theoretical analysis. *Meas. Sci. Technol.*, 9:232–9, 1998.
- [11] Drandova, Gergana. *NMR Investigation in Copper-Oxide Chain Compounds and High- $T_c$  Superconductors*. PhD thesis, University of Texas at Austin, 2001.
- [12] Dubois, J.G.A., Gerritsen, J.W., Hermsen, J.G.H., van Kempen, H. A low temperature scanning tunneling microscope for use in high magnetic fields. *Rev. Sci. Instrum.*, 66:4146–49, 1995.
- [13] Fukushima, E. and Roeder, S. *Experimental Pulse NMR, A Nuts and Bolts Approach*. Addison-Wesley, 1981.
- [14] Garbini, J.L., Bruland, K.J., Dougherty, W.M., Sidles, J.A. Optimal control of force microscope cantilevers. i. controller design. *J. Appl. Phys.*, 80:1951–8, 1996.
- [15] Garner, S. *Force-gradient detection of nuclear magnetic resonance*. PhD thesis, Cornell University, 2005.

- [16] Garner, S., Kuehn, S., Dawlaty, J., Jenkins, N., Marohn, J. Force-gradient detected nuclear magnetic resonance. *Appl. Phys. Lett.*, 84:5091–5093, 2004.
- [17] Graf, Tobias. Interferometry on high-q double torsional oscillators for the study of vortices in type-ii superconductors. Master’s thesis, The University of Texas at Austin, 1998.
- [18] Halliday, D., Resnick, R., Krane, K. *Physics, Vol. 2*. John Wiley & Sons, Inc., 1992.
- [19] Hug, H.J., Stiefel, B., van Schendel, P.J.A., Moser, A., Martin, S., Guntherodt, H.-J. A low temperature ultrahigh vacuum scanning force microscope. *Rev. Sci. Instrum.*, 70:3625–40, 1999.
- [20] Hutter, J. and Bechhoefer, J. Calibration of atomic-force microscope tips. *Rev. Sci. Instrum.*, 64:1868–73, 1993.
- [21] Jenkins, N., et al. Batch fabrication and characterization of ultrasensitive cantilevers. *Journal of Vacuum Science & Technology B*, 22:909–915, 2004.
- [22] Kleiman, R.N., Kaminsky, J., Reppy, J.D., Pindak, R., Bishop, D.J. Single-crystal silicon high-q torsional oscillators. *Rev. Sci. Instrum.*, 56:2088–2091, 1985.
- [23] Klein, O., Naletov, V.V., Alloul, H. Mechanical detection of nuclear spin relaxation in a micron-size crystal. *Eur. Phys. J., B*, 17:57–68, 2000.

- [24] Kuehn, S., Loring, R., Marohn, J. Dielectric fluctuations and the origins of non-contact friction. *Phys. Rev. Lett.*, 96:156103, 2006.
- [25] Kuehn, S., Marohn, J., Loring, R. Non-contact dielectric friction. *J. Phys. Chem. B*. Accepted for publication.
- [26] Kydon, D.W., Petch, H.E., Pintar, M. Spinlattice relaxation times in deuterated ferroelectric ammonium sulfate and fluoroberyllate. *J. of Chem. Phys.*, 51:487–91, 1969.
- [27] Landau, L.D. and Lifshitz, E.M. *Mechanics, 3rd Ed.* Pergamon Press, 1976.
- [28] Lin, Q., Degen, C., Tomaselli, M., Hunkeler, A., Meier, U., Meier, B. Magnetic double resonance in force microscopy. *Phys. Rev. Lett.*, 96:137604, 2006.
- [29] Mamin, H.J., Rugar, D. Sub-attoneutron force detection at millikelvin temperatures. *Appl. Phys. Lett.*, 79:3358–3360, 2001.
- [30] Marion, J.B. and Thornton, S. *Classical Dynamics of particles and Systems, 4th Ed.* Saunders College Pub., 1995.
- [31] Marohn, J., Fainchtein, R., Smith, D. Mechanical modulation of sample magnetization in magnetic resonance force microscopy. *J. Appl. Phys.*, 86:4619–25, 1999.

- [32] Marohn, J., Fainchtein, R., Smith, D. Mechanical modulation of sample magnetization in magnetic resonance force microscopy. *J. Appl. Phys.*, 86:4619–25, 1999.
- [33] Miller, C. *Nuclear Magnetic Resonance Force Microscopy: Adiabaticity, External Field Effects and Demonstration of Magnet-on-Oscillator Detection with Sub-Micron Resolution*. PhD thesis, The University of Texas at Austin, 2003.
- [34] Mirsaidov, U. *Force Detected Nuclear Resonance Force Microscopy*. PhD thesis, The University of Texas at Austin, 2005.
- [35] Oppenheim, A.V. and Schafer, R.W. *Digital Signal Processing*. Prentice-Hall, 1975.
- [36] Rugar, D., Budaklan, R., Mamin, H.J., and Chui, B.W. Single spin detection by magnetic resonance force microscopy. *Nature*, 430:329–332, 2004.
- [37] Rugar, D., Mamin, H. J., Erlandsson, R., Stern, J. E., Terris, B. D. Force microscope using a fiber-optic displacement sensor. *Rev. Sci. Instrum.*, 59:2337–40, 1988.
- [38] Rugar, D., Yannoni, C.S., Sidles, J.A. Mechanical detection of magnetic resonance. *Nature*, 360:563–6, 1992.
- [39] Sidles, J.A. Noninductive detection of single-proton magnetic resonance. *Appl. Phys. Lett.*, 58:2854–2856, 1991.

- [40] Slichter, C. *Principles of Magnetic Resonance, 3rd Ed.* Springer-Verlag, 1990.
- [41] Smith, D.D., Marohn, J.A., Harrell, L.E. Detailed description of a compact cryogenic magnetic resonance force microscope. *Rev. Sci. Instrum.*, 72:2080–2089, 2001.
- [42] Stark, R., Drobek, T., Heckl, W. Thermomechanical noise of a free v-shaped cantilever for atomic-force microscopy. *Ultramicroscopy*, 86:207–15, 2001.
- [43] Stipe, B.C., Mamin, H.J., Stowe, T.D., Kenny, T.W., Rugar, D. Magnetic dissipation and fluctuations in individual nanomagnets measured by ultrasensitive cantilever magnetometry. *Phys. Rev. Lett.*, 86:2874–7, 2001.
- [44] Stowe, T.D., Yasumura, K., Kenny, T.W., Botkin, D., Wago, K., Rugar, D. Attonewton force detection using ultrathin silicon cantilevers. *Appl. Phys. Lett.*, 71:288–290, 1997.
- [45] Streckeisen, P., Rast, S., Wattering, C., Meyer, E., Vettiger, P., Gerber, C., Guentherodt, H.J. Instrumental aspects of magnetic resonance force microscopy. *Applied Physics A*, 66:S341, 1998.
- [46] Philips Medical Systems. *Principles of MR Imaging.* Philips Medical Systems, 1984.



- [47] Villa. P, Vaquero, J.J., Chesnick, S., Ruiz-Cabello, J. Probe efficiency improvement with remote and transmission line tuning and matching. *Magn. Reson. Imaging*, 17:1083–6, 1999.
- [48] Volodin, A., Buntinx, D., Brems, S., Van Haesendonck, C. Piezoresistive mechanical detector for magnetic resonance force microscopy. *Rev. Sci. Instrum.*, 76:63705,1–5, 2005.
- [49] Wago, K., Zuger, O., Kendrick, R., Yannoni, C.S., Rugar, D. Low-temperature magnetic resonance force detection. *Journal of Vacuum Science & Technology B*, 14:288–290, 1997.
- [50] Welch, P.D. The use of fast fourier transform for the estimation of power spectra: A method based on time averaging over short, modified periodograms. *IEEE Trans. Audio Electroacoust.*, AU-15:70–3, 1967.
- [51] Yasumura, K. *Energy Dissipation Mechanisms in Microcantilever Oscillators with Applications to the Detection of Small Forces*. PhD thesis, Stanford University, 2001.
- [52] Zhang, Z., Hammel, P.C. Magnetic resonance force microscopy with a ferromagnetic tip mounted on the force detector. *Solid State Nuclear Magnetic Resonance*, 11:65–72, 1998.

# Index

- 3-Axis Piezoelectric Positioners*, 47
- Abstract, vii
- Acknowledgments*, v
- Appendices*, 76
- Appendix
- Feedback Electronics*, 77
  - Frequency Modulation Electronics*, 88
  - Inertial Positioner Driver Electronics*, 81
- Bibliography*, 99
- Bloch Equations*, 5
- Cantilever*, 28
- Cantilever Dynamics*, 20
- Characterization*, 35
- Cyclic Adiabatic Inversion of Magnetization*, 16
- Dedication*, iv
- Equation of Motion of Isolated Spins in Magnetic Field*, 3
- Errata in Oxford's HelioxVL  $^3\text{He}$  Insert Manual*, 92
- Experiments*, 52
- Fabrication*, 30
- Fiber Optic Interferometer*, 39
- Force Detected Magnetic Resonance*, 16
- Future Directions*, 71
- Initial Attempt to Observe Force-detected MRFM*, 55
- Introduction*, 1
- Introduction to double torsional oscillators*, 29
- Magnetic Field Gradient*, 52
- Magnetic Resonance Force Microscopy*, 15
- Measuring  $T_1$  and  $T_2$  with MRFM*, 24
- Measuring Relaxation in pulsed NMR*, 11
- Modifications to the Experimental Setup*, 71
- MRFM Instruments*, 28
- Nuclear Magnetic Resonance*, 3
- Phase Cycling*, 72
- Pulsed NMR*, 8
- RF components*, 44
- Rotating Frame*, 10
- Spin Nutation and Calibration of  $B_1$* , 26
- Theoretical Foundations*, 3
- Troubleshooting*, 59

# Vita

Yong Joong Lee was born in Daejeon, Republic of Korea on 28 July 1976, the son of Rev. Do Ung Lee and Dong Sik Cho. His family came to the United States in 1991 just short of the completion of his middle school education. His family settled in Texas and he attended high school and college in Texas. He received the Bachelor of Science degree in physics and the Bachelor of Arts degree in mathematics from the University of Texas in May 1999. He was accepted to graduate school and started graduate studies in physics in August 1999. Soon afterwards he started working in Prof. John Markert's laboratory for the construction of a low temperature nuclear magnetic resonance force microscope.

Permanent address: 11901 Hobby Horse CT APT 1737  
Austin, Texas 78758

This dissertation was typeset with L<sup>A</sup>T<sub>E</sub>X<sup>†</sup> by the author.

---

<sup>†</sup>L<sup>A</sup>T<sub>E</sub>X is a document preparation system developed by Leslie Lamport as a special version of Donald Knuth's T<sub>E</sub>X Program.